DEVELOPMENTS IN MODELLING AND SIMULATION..JAPAN, SOUTH KOREA AND CHINA

Genetic effects of dynamic recrystallization on ductile fracture at elevated temperature for AA7075 alloy with various stress states: modeling and simulation

Bingtao Tang[1,2] · Mian Li[1,2] · Ning Guo[1,2] · Qianchi Li[1,2] · Lu Han[3] · Zhongguo Zhang[4]

Abstract

Temperature and strain rate related dynamic recrystallization (DRX) and its inherited effects on ductile fracture have become an urgent issue which impede accurate prediction of fracture strain and restrict formability for 7075 aluminum alloy in hot deformation process. In order to precisely elaborate the ductile fracture behavior of 7075 aluminum alloy during hot forming process and accurately predict the initiation of ductile fracture, an extended ductile fracture criterion (DFC) at elevated temperature was established considering DRX effects and various stress states. The relationship between fracture strain and Z parameter is revealed in DRX and DRX-free region, respectively. It is noted that fracture strain decreases with the increasing Z parameter in DRX region, while Z parameter has little effect on the fracture behavior in DRX-free region. Consequently, the Z parameter embedded DRX model is introduced into the modified Mohr–Coulomb (MMC) DFC under distinct stress states at elevated temperatures for 7075 aluminum alloy. Based on the Abaqus/Explicit platform, the proposed ductile fracture model is implemented in finite element simulation via VUMAT. Hot forming of T-shaped parts is carried out, and the predicted fracture scenarios including damage evolution, volume fraction of DRX are validated by experimental results.

Keywords 7075 aluminum alloy · Zener-Hollomon parameter · Stress state · DRX · Ductile fracture

Highlights

• An extended ductile fracture criterion at elevated temperature was established considering DRX effects and various stress states.
• Fracture strain decreases with the increasing Z parameter in DRX region, while little impact in DRX-free region.
• The influence of process parameters on the formability of T-shaped parts are predicted.
• DRX and its inherited effects on ductile fracture have been revealed for AA7075 alloy in hot deformation process.

✉ Ning Guo
guoning19891227@163.com

✉ Lu Han
jl.wang@connect.polyu.hk

1   School of Mechanical Engineering, Qilu University of Technology (Shandong Academy of Sciences), Jinan 250353, China

2   Shandong Institute of Mechanical Design and Research, Jinan 250103, China

3   Key Laboratory of High Efficiency and Clean Mechanical Manufacture of Ministry of Education, School of Mechanical Engineering, National Demonstration Center for Experimental Mechanical Engineering Education, Shandong University, Jinan 250061, China

4   Shandong Toget Brake System Co. Ltd., Zaozhuang 277400, China

Introduction

In the last decade, 7075 aluminum alloys have attracted the attention of many researchers as an alternative to high-strength steels due to their excellent strength-to-density ratio, bending stiffness and corrosion resistance. The integration of formability defects and performance control of 7075 aluminum alloy with high strength and toughness lightweight in hot stamping forming process is the most critical issue which restricts the mass production of curved

thin-wall components in new energy vehicle (NEV) body. However, the intrinsic mechanisms resulting in the inhomogeneous deformation and ductile fracture under the varying temperatures and transient stamping rates are still not quite clear. Additionally, the existing phenomenological DFCs in predicting the fracture strain lack the essential development considering microstructural evolution such as DRX formation and complex stress states.

To improve the prediction accuracy of fracture strain, hydrostatic stress, principal stress and shear stress, associated with Lode parameter, were considered in modeling the coupled and uncoupled DFCs [1–3]. The energy criterion was firstly postulated by Ma et al. [4], in which once the plastic work per unit volume of metallic materials exceeded a threshold value, the ductile fracture would occurred. In addition, the occurrence of ductile fracture was driven by the first principal stress, as described by Cockcroft and Latham [5]. Furthermore, stress triaxiality was recognized as an important role in ductile failure and particularly Rice and Tracey [6] found that the rates of void growth and aggregates were promoted by stress triaxiality at high levels. According to the experiment results, a ductile fracture model associated with stress triaxiality was presented. Several modified DFCs including Lode parameter were proposed to improve the prediction accuracy of ductile fracture in depth. Xue [7] first considered the Lode angle effect due to the contradiction that the equivalent plastic strain of pure shear fracture was smaller than that of uniaxial tensile fracture. Bai and Wierzbicki [8] introduced the normalized Lode angle effect, and a new asymmetric 3D fracture locus, in the space of equivalent fracture strain, stress triaxiality and the Lode angle parameter, was developed. Lou and Huh [9] used the technique of the Mohr 's circles to transform the Mohr–Coulomb criterion into the space of equivalent fracture strain, stress triaxiality and the Lode parameters. The fracture strain predicted by the DFCs considering Lode parameter had transformed into a complicated three-dimensional plane rather than a single curve plotted a two-dimensional plane. In addition, Lou et al. [10] proposed a model related to stress triaxiality and Lode parameters to predict ductile fracture strain using maximum shear stress, in which a constant value of -1/3 for cut-off value of the stress triaxiality was employed. Furthermore, Lou and Huh [11] proposed the Lode parameter-based DFCs. In their work, it was noted that the fracture positions had a good agreement with the characterization of fracture morphology by SEM imaging except for positions with high stress triaxiality. Moreover, Lou et al. [12] optimized the fracture criterion to enhanced the prediction accuracy of the new criterion for the balanced biaxial tensile stress state. Comparatively, the modified Mohr–Coulomb model (MMC) proposed by Bai and Wierzbicki [13] showed a considerable performance in predicting ductile fracture strain in a wide range of stress triaxialities for metallic materials. Although the MMC criterion initially represents the fracture response of geo-material, the MMC criterion was validated by many other different metallic materials. Jia and Bai [14, 15] developed an anisotropic MMC ductile fracture model in strain space to predict the ductile failure behavior of AZ31B-H24 magnesium alloy sheets. Qian et al. [16] predicted the tensile and shear fractures of 5083-O aluminum alloy by using a phenomenological MMC fracture criterion. Tang et al. [17] developed an anisotropic MMC ductile fracture criterion, which utilized a fourth order linear transformation strain tensor to account for anisotropic damage, so as to simulate the Ti-6Al-4 V anisotropic ductile fracture at room temperature under various stress states along RD, DD and TD. Furthermore, the different fracture modes with a large range of stress triaxiality for a shear-punch test was successfully predicted by Qian et al. [18] using MMC fracture model.

It is well-known that most of the above-mentioned DFCs are focused on ductile fracture prediction at room temperature and few of them emphasis on the fracture behavior at elevated temperature[19–22]. Tian and Guo [23] studied the effects of stress triaxiality, Lode angle, temperature and strain rate on the fracture properties of 6061-T651 aluminum alloys. It is found that the predicted results of the MMC fracture criterion related to the Lode angle are closer to the experimental results than the fracture criterion independent of the Lode angle. Since the ductile fracture behavior of metallic materials was significantly affected by the forming temperature and strain rate, several modified DFCs had incorporated with temperature and strain rate effects via introducing the parameter of Zener-Hollomon, simplified as Z parameter [24, 25]. In virtue of the Z parameter, Zhang et al. [26] developed an improved Oyane fracture criterion for Ti40 alloy by introducing the effects of deformation temperature and strain rate on cracks initiation. Hashemi et al. [27] used the DFC at elevated temperature to predict the bulge height of 6063 aluminum tube, which was calibrated in different stress states by means of various uniaxial tensile tests at distinct temperatures and strain rates. Kim et al. [28] established a fracture criterion and proved the fracture behavior was close correlated with the Z parameter. However, the DFCs with Z parameter only described the relationship between ductile fracture strain and temperature/strain rate effects during hot plastic deformation process, ignoring the influence of microstructural evolution on ductile fracture behavior. In view of this issue, Shang et al. [29] suggested that the DRX of as-forged 316LN austenitic stainless steels was considered as a significant deformation mechanism and was introduced into DF2015 fracture model to simulate ductile fracture in hot forming of 316LN stainless steel. Dehghan et al. [30] studied the hot deformation behavior of 304 austenitic stainless steel and described the evolution of the DRX structure. Zhang

et al. [31] developed a model to systematically investigate the effects of strain, strain rate and deformation temperature on the microstructure evolution, and further to simulate the DRX process of 7085 aluminum alloy. During the hot deformation process of 7075 aluminum alloy, the grain size and degree of DRX increased with the increase of temperature and the decrease of strain rate. This issue shows the typical characteristics of continuous DRX, which has a great influence on the strength, hardness and plasticity of the material [32]. Consequently, there is an urgent requirement to consider the temperature, strain rate and DRX effects in predicting ductile fracture of aluminum alloys in hot forming process.

In this study, various types of tensile tests with different specimen configurations were firstly performed at room temperature to obtain varying stress states and proportional loading paths. Furthermore, the evolution of the critical fracture strain and DRX was computed by considering the numerical simulation method and physical experiments. A temperature-and strain rate-dependent fracture criterion, named as extended MMC model, was developed by incorporating the effect of DRX in hot plastic deformation process of aluminum alloy. Finally, validations were carried out to evaluate the accuracy of the fracture criterion by simulating the influence of hot stamping temperature and speed on the ductile fracture of T-shaped parts.

Experimental methodology

Tensile tests at room temperature

To study the effects of different stress states on ductile fracture of 7075 aluminum alloy, several types of tensile tests were conducted under quasi-static loading conditions at room temperature. This type of test was intended to evaluate the ductility of 7075 aluminum alloy under various stress states performed on a universal testing machine [33, 34].

The AA7075-T6 alloy sheet with a thickness of 1.5 mm was used as the case study material. The specimen geometry is illustrated in Fig. 1. The dog-bone, central holes, notched, in-plane shear and Nakajima specimens representing five stress states, were produced by a wire electrical discharge machining and employed in a variety of tensile tests respectively. The elongation between measured points and the entire strain field was recorded by the two-dimensional digital imaging correlation (DIC) software ARAMIS 2017. In order to explore the ductile fracture evolution under different stress states, a universal testing machine (UTM) was selected to conduct the tensile tests at room temperature. In addition, Genbon EC600 hydraulic machine was employed to conduct the Nakajima test to reveal the evolution of ductile fracture in balanced biaxial stress state. The loading speed for the tested samples were shown in Table 1. Particularly, the force–displacement curves as well as the strain

Fig. 1 Specimens with different stress states: (**a**) Dog-bone specimen, (**b**) specimen with a central hole, (**c**) notched specimen, (**d**) in-plane shear specimen, (**e**) Nakajima specimen

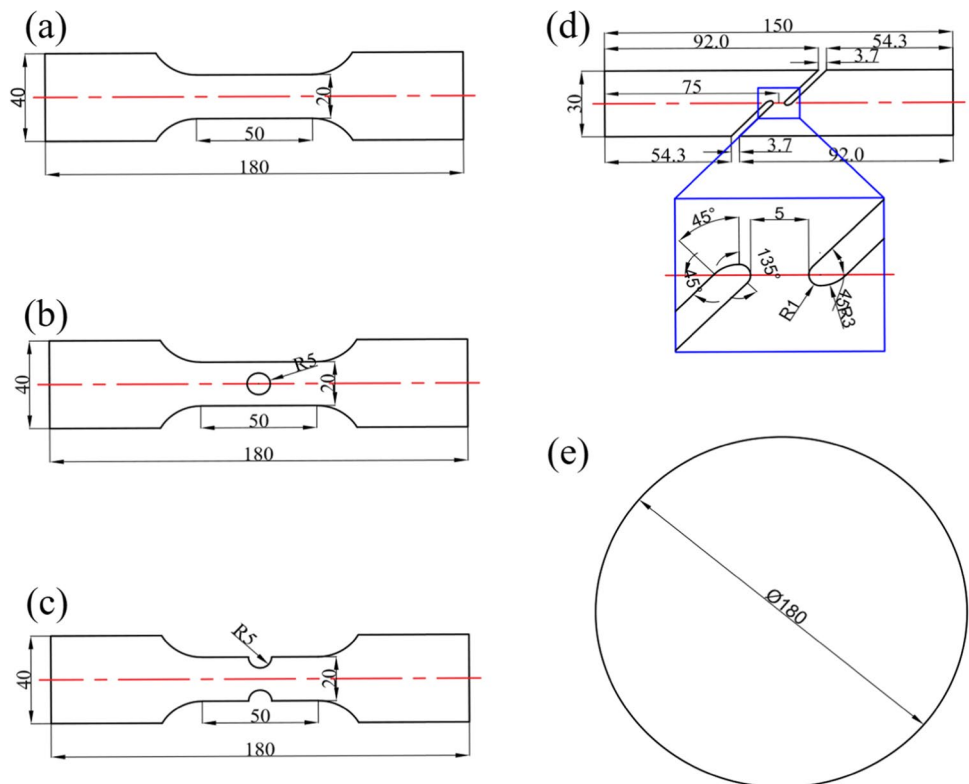**Table 1** The velocity of the crosshead for various tensile specimens (mm/min)

Dog-bone	Central hole	Notched	In-plane shear	Nakajima
1	0.3	0.5	0.6	0.25

field were measured synchronously by the testing machine and the DIC system. The data in the stretching process was put into the ARAMIS system through the force sensor, and the load–displacement curve was synthesized with the displacement data obtained by adding a virtual extensometer in the ARAMIS system through post-processing. Binocular cameras recorded images at a speed of 5 Hz, and the resolution of the DIC images was set to 2750×2200.

Z parameters determination and DRX characterization at elevated temperature

In order to find the relationship between ductile fracture strain and process parameters, hot tensile tests at elevated temperature were conducted at 623, 673 and 723 K with the strain rates of 0.01, 0.1 and 1 s^{-1} along the rolling direction. The dimensions of tensile specimen were shown in Fig. 2(a). In order to determine the relationship between Z parameters and DRX, hot compression tests, shown in Fig. 3. were carried out. The dimension of specimens used in compression tests was exhibited in Fig. 2(b). A series of compression tests were conducted on specimens at 573, 623, 673 and 723 K with the strain rates of 0.01, 0.1, 1 and 5 s^{-1} along the rolling direction.

In the EBSD measurement, the longitudinal sections of dog-bone specimens were polished sequentially with 400 and 1200 grit SiC abrasive papers followed by polishing using diamond paste and colloidal silica solution. To obtain the EBSD patterns, the samples were electro-polished using a solution consisting of 78 ml perchloric acid (60%), 730 ml ethanol (96%), 100 ml butoxyethanol and 90 ml distilled water. The electro-polishing was conducted at 12-15 V for 10 s.

The lower the strain rate, the more complete the DRX behavior of the material, and the recrystallization nucleation can be observed more intuitively. Figure 4. shows the EBSD micrograph of 7075 aluminum alloy with strain rate 0.01 s^{-1}, the volume fraction of DRX region

Fig. 2 Dimensions of specimens employed in (**a**) Hot tensile and (**b**) hot compression tests (unit: mm)
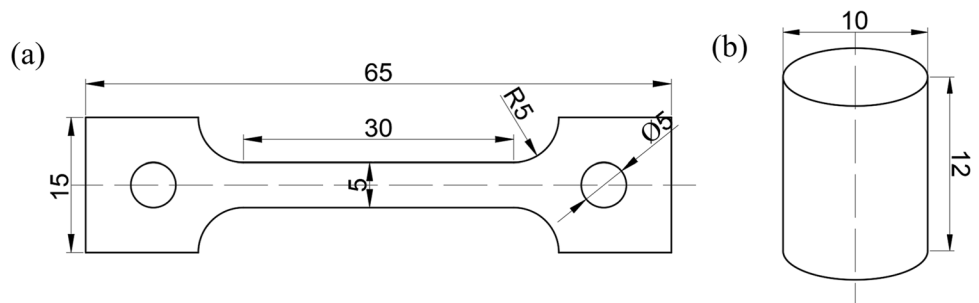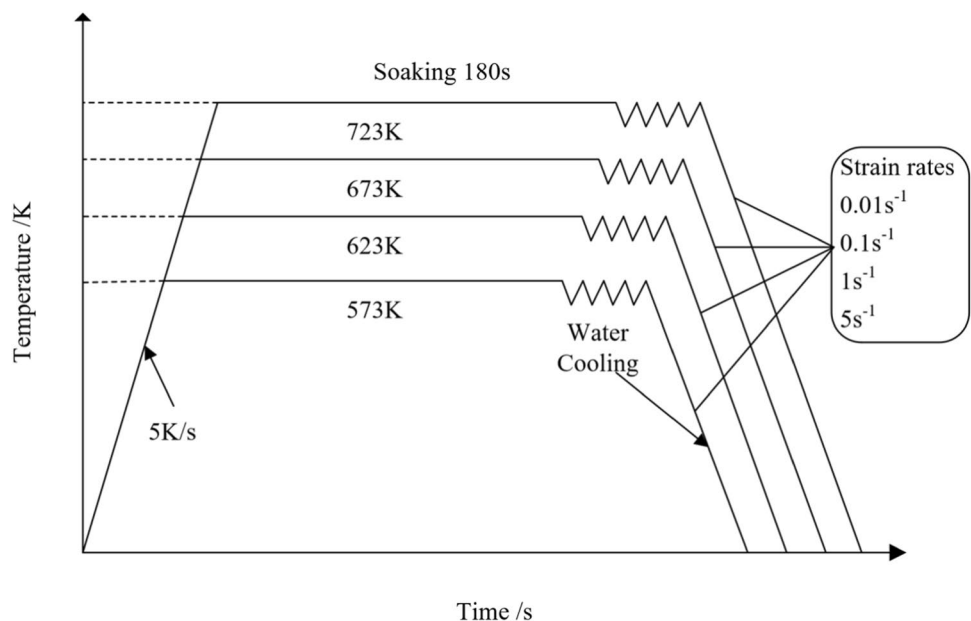

Fig. 3 Flow chart of the Gleeble compression test procedure, which consists of four steps: heating, soaking, isothermal deformation and water cooling
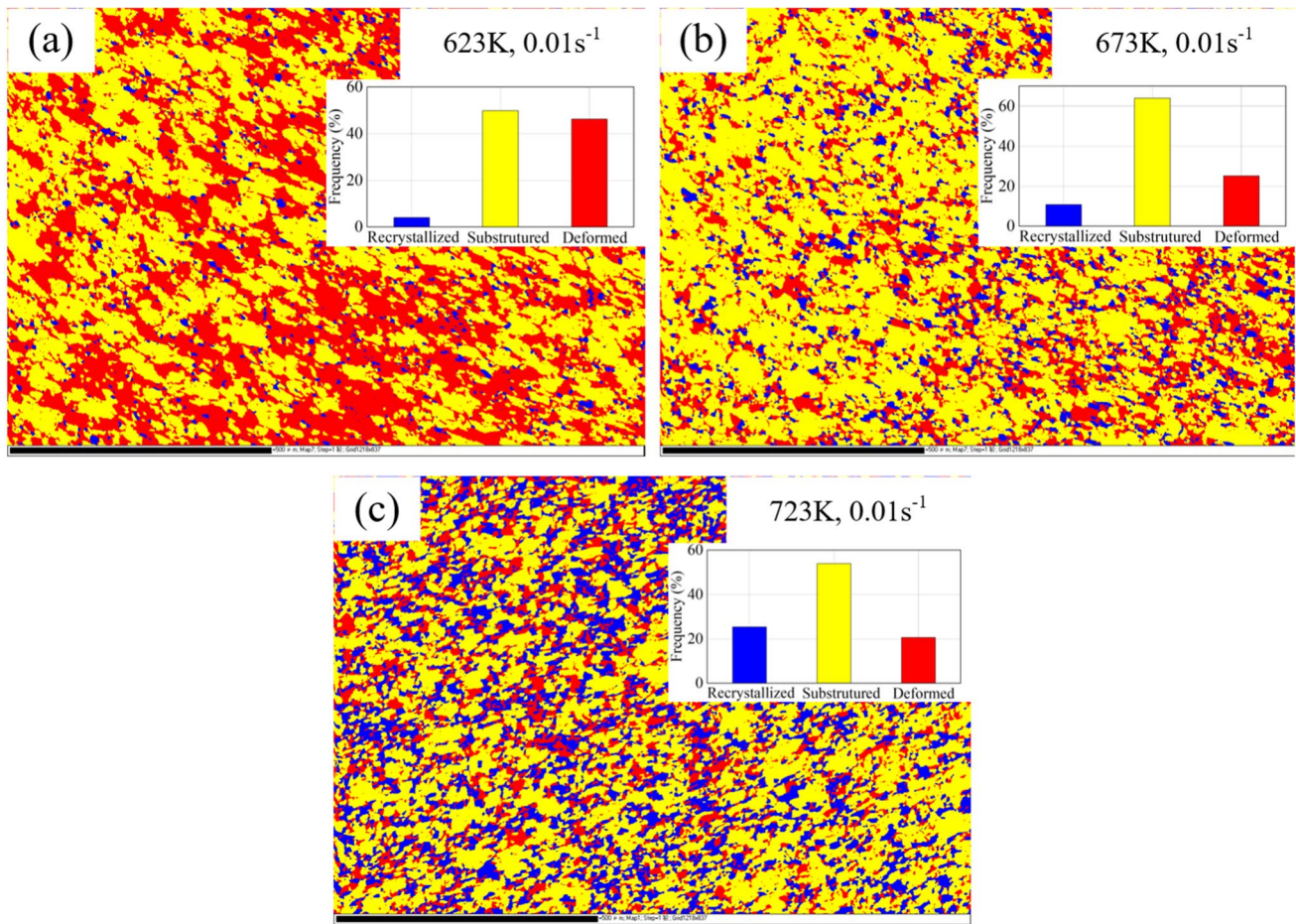
Fig. 4 EBSD micrographs of 7075 aluminum alloy deformed at: (**a**) 623 K and 0.01 s^{-1}, (**b**) 673 K and 0.01 s^{-1}, (**b**) 723 K and 0.01 s^{-1}

rises with the increase of forming temperature. It is well known that nucleation of recrystallize grains is mainly dominated by temperature and strain rate. Particularly, dislocations have adequate time to move which causes the nucleation of newly refined grains at high temperature and low strain rate. However, with the increase of strain rate, the migration rate of grain boundaries slows down, which leads to a decrease of the volume fraction of DRX. Figure 5 shows the grain morphology including DRX, subgrains and deformed grains at strain rates of 0.01, 0.1 and 1 s^{-1} with temperature of 723 K. It is noted that with the rise of strain rate, the proportion of the low angle grain boundary increases indicating that the volume fraction of DRX decreases with the rise of strain rate. It is caused by the fact that a certain number of dislocations move and further transform into low angle grain boundary by absorbing dislocations around them, which form the new subgrains [35–39].

DRX and Z parameter dependent MMC model

Considering the effect of temperature and strain rate on ductile fracture, Johnson and Cook [40] established the classical DFC called Johnson–Cook (J-C) model based on the damage accumulation theory:

$$\overline{\varepsilon_f} = \left[D_1 + D_2 exp\left(D_3 \eta\right) \right]\left[1 + D_4 ln\dot{\varepsilon}^* \right]\left[1 + D_5 T^* \right] \tag{1}$$

with $D_1 - D_5$ denote material constants; η represents stress triaxiality, $\dot{\varepsilon}^*$ denotes the dimensionless strain rate given by $\dot{\varepsilon}^* = \dot{\varepsilon}/\dot{\varepsilon}_0$, $\dot{\varepsilon}$ and $\dot{\varepsilon}_0$ are the strain rate at any time and reference strain rate, respectively, T^* indicates the dimensionless temperature calculated by $T^* = \left(T - T_0\right)/\left(T_m - T_0\right)$, in which T is the actual temperature, T_0 is the room temperature and T_m is the melting temperature, $\overline{\varepsilon}_f$ is fracture strain. The J–C model not only takes into account the influence of
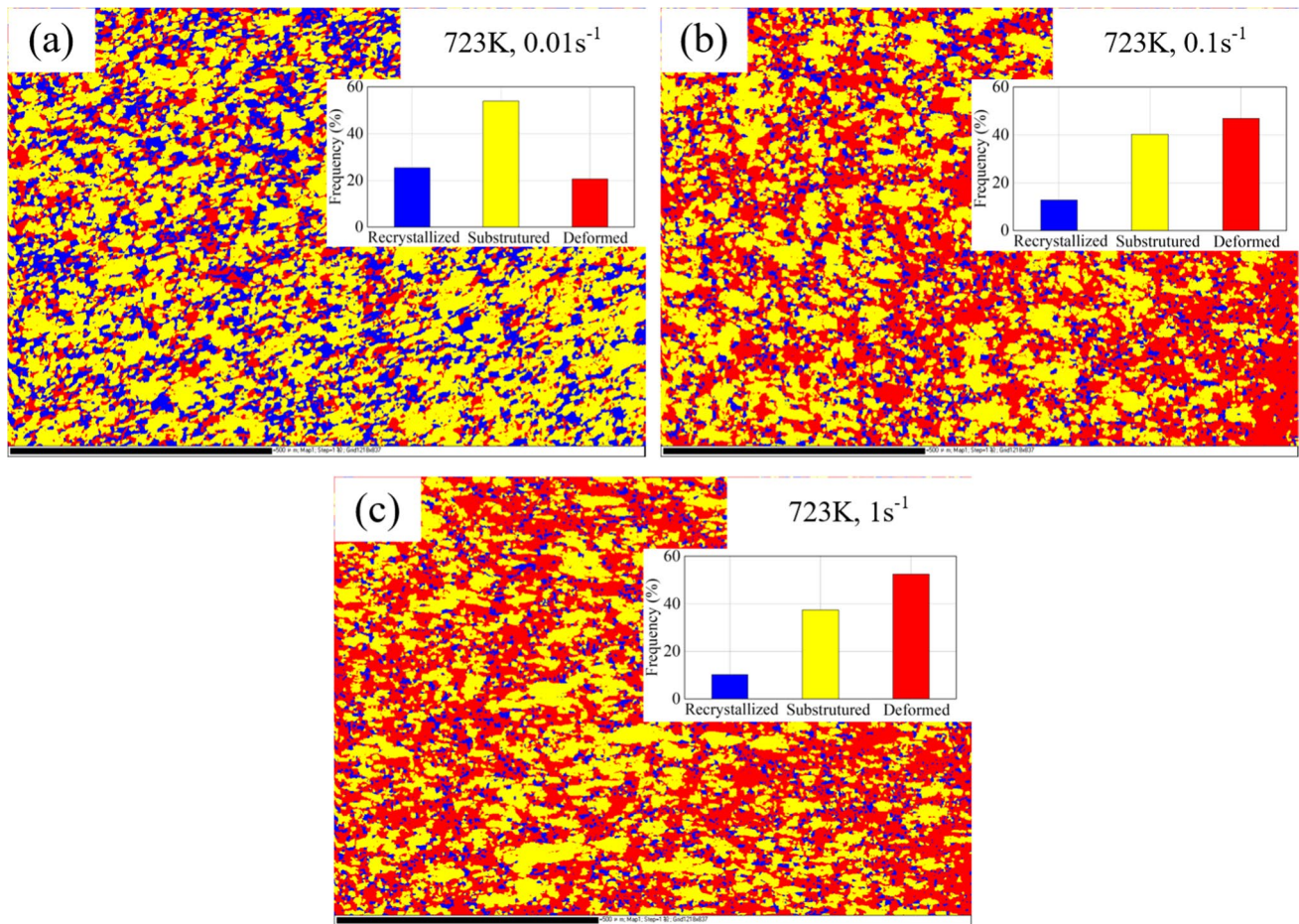
Fig. 5 EBSD micrographs of 7075 aluminum alloy deformed at: (**a**) 723 K and 0.01 s^{-1}, (**b**) 723 K and 0.1 s^{-1}, (**b**) 723 K and 1 s^{-1}

hydrostatic pressure, but also the effects of strain rate and temperature on fracture. The functional relationship between critical fracture strain and stress triaxiality are obtained. But it lacks the influence of Lode parameter on fracture strain.

Compared with the J–C model, Bai and Wierzbicki [13] proposed a new uncoupled ductile fracture criterion to depict the ductile fracture behavior of metallic materials, in which stress triaxiality and Lode angle parameters were introduced based on the Mohr–Coulomb criterion. Lou and Huh [9] converted this fracture criterion to $(\eta, L, \overline{\varepsilon}^p)$ space:

$$\overline{\varepsilon}_f = [\frac{K}{c\cos\varphi}(\frac{1}{\sqrt{L^2+3}} + (\eta - \frac{L}{3\sqrt{L^2+3}})\sin\varphi) \\ (c_\theta^s + (2 + \sqrt{3})(c_\theta^{ax} - c_\theta^s)(\sqrt{L^2+3} - \sqrt{3}))]^{-\frac{1}{n}} \quad (2)$$

where K, c, φ, c_θ^s, c_θ^s, n denote material constants, η indicates the stress triaxiality which is defined by $\sigma_m/\tilde{\sigma}$, in which σ_m represents the mean stress defined by the average value of the three principal stress, i.e., $\sigma_m = (\sigma_1 + \sigma_2 + \sigma_3)/3$, $\tilde{\sigma}$ is mises equivalent stress. L is the Lode parameter given by $(2\sigma_2 - \sigma_1 - \sigma_3)/(\sigma_1 - \sigma_3)$.

During the hot plastic deformation of metallic materials, the mechanical properties especially the ductile fracture behavior are significantly affected by DRX evolution [41]. Moreover, it is noted that the occurrence of DRX is relative to the variation of deformation temperature and strain rate [42, 43]. In consideration of this issue, Z parameter is comprehensively employed in the characterization of the comprehensive effect of temperature and strain rate on plastic deformation behavior such as DRX, which is computed in Eq. (3):

$$Z = \dot{\varepsilon}\exp\left(\frac{Q_{act}}{RT}\right) = A\left(\sin h\left(\alpha\sigma_p\right)\right)^{n_1} \quad (3)$$

with T denotes the temperature (the Kelvin) and, R represents the gas constant (8.314 J/(mol•K)), $\dot{\varepsilon}$ is the strain rate, Q_{act} characterizes the activation energy, σ_p is the peak stress, A, α and n_1 are material constants.

It is noted that fracture strain is independent of Z parameter in DRX-free region during hot plastic deformation process, which is similar to that at room temperature. Once DRX initiates, the fracture strain increases linearly in a

certain range with the decrease of the logarithm of Z parameter. Therefore, the fracture strain is classified according to different DRX conditions [44], and the relationship between fracture strain and Z parameters can be depicted as follows:

$$\begin{cases} \overline{\varepsilon}_{hf} = \varepsilon_{rf} & \text{Without DRX} \\ \overline{\varepsilon}_{hf} = \varepsilon_{rf}\left[A_f - B_f * \ln(Z)\right] & \text{DRX region} \end{cases} \quad (4)$$

with $\overline{\varepsilon}_{hf}$ denotes the fracture strain at elevated temperature, A_f and B_f represent material constants, ε_{rf} is the fracture strain measured at room temperature. In order to characterize DRX initiation, the critical strain ε_c is denoted as the representative parameter.

In the hot plastic deformation process with fixed temperature and strain rate, DRX is not prone to occurring at the beginning of deformation, while the degree of DRX increases with the rise of strain [45]. To represent the dynamic evolution of DRX during hot plastic deformation process and to reveal its influence on ductile fracture, X_{drx} is used as a weight function to measure the volume fraction evolutions of DRX in the specimen in case of the hot compression. The volume fraction of DRX is defined as the volume ratio of recrystallized grains to the total volume ratio of all grains [26]. Then X_{drx} is formulated as:

$$X_{drx} = 1 - \exp\left[-k_d\left(\frac{\varepsilon - \varepsilon_c}{\varepsilon_p}\right)^{n_d}\right] \quad (5)$$

where X_{drx} denotes the volume fraction of recrystallized grains, k_d and n_d represent the Avrami's constants, ε_p indicates the peak strain.

Then the fracture strain at elevated temperature can be summarized as:

$$\begin{cases} \overline{\varepsilon}_{hf} = [\frac{K}{c\cos\varphi}(\frac{1}{\sqrt{L^2+3}} + (\eta - \frac{L}{3\sqrt{L^2+3}})\sin\varphi)(c_\theta^s + (2+\sqrt{3}) \\ \quad (c_\theta^{ax} - c_\theta^s)(\sqrt{L^2+3} - \sqrt{3}))]^{-\frac{1}{n}} \quad \varepsilon < \varepsilon_c \\ \overline{\varepsilon}_{hf} = [\frac{K}{c\cos\varphi}(\frac{1}{\sqrt{L^2+3}} + (\eta - \frac{L}{3\sqrt{L^2+3}})\sin\varphi)(c_\theta^s + (2+\sqrt{3}) \\ \quad (c_\theta^{ax} - c_\theta^s)(\sqrt{L^2+3} - \sqrt{3}))]^{-\frac{1}{n}}[(1 - X_{drx}) \\ \quad + (A_f - B_f * \ln(Z))X_{drx}] \quad \varepsilon \geq \varepsilon_c \end{cases}$$

$$(6)$$

Calibration

Relationship between fracture strain and stress state at room temperature

Figure 6 shows the equivalent stress–strain curve using the reverse engineering method for 7075 aluminum alloy at room temperature under quasi-static loading, which was utilized as input parameters for the FE simulations of various types of tensile tests at room temperature [46]. The
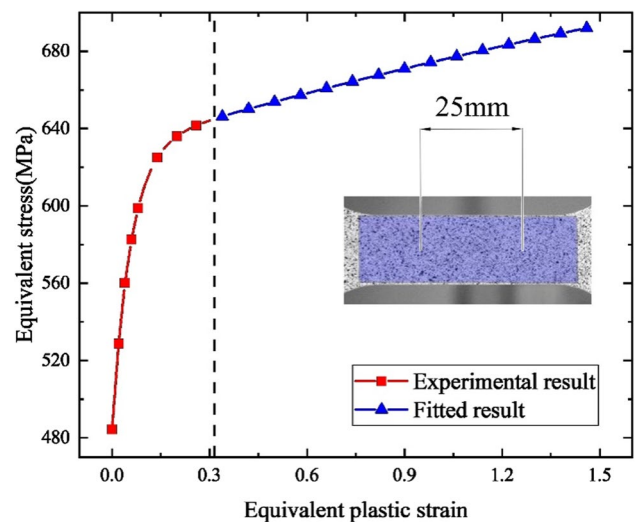
Fig. 6 Flow stress curve of 7075 aluminum alloy at room temperature and under quasi-static loading condition

reliability of the calibrated stress–strain relationship was verified by comparing the numerical and experimental load–displacement curves shown in Fig. 9.

The modified ductile fracture model developed in Eq. (6) has eight material parameters to be calibrated, i.e., K, c,φ, c_θ^s, c_θ^s, n, A_f, B_f. It should be noted that K, c,φ, c_θ^s and n are material parameters related to stress state which could be calibrated by tensile experiments with different stress triaxiality and Lode parameters at room temperature, as illustrated in Fig. 7, while A_f and B_f are material parameters related to temperature. It is noted that in Fig. 7 the central hole specimen, the notched specimen, the in-plane shear specimen and the Nakajima specimen represent the uniaxial, plane strain, pure shear and equal-biaxial stress state, respectively.
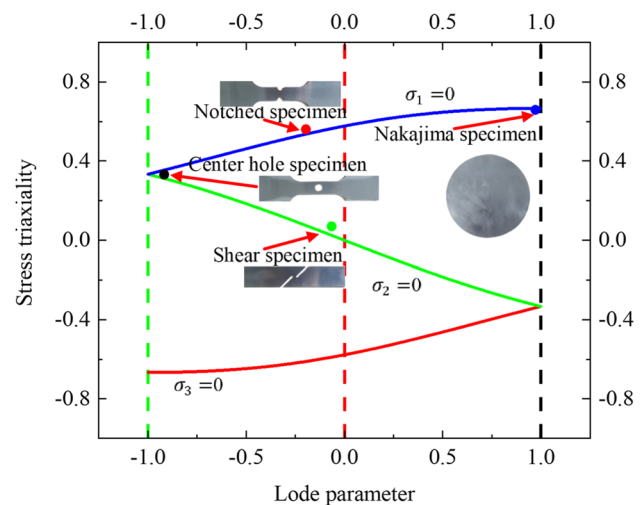
Fig. 7 Stress states expressed in the space of $\langle\eta, L\rangle$

A hybrid calibration method including FE simulations and uniaxial tensile tests were designed to determine the material parameters.

In the finite element modeling, Young's modulus is 71GPa and Poisson's ratio is 0.3. All specimens in Fig. 8 with different stress states were meshed using C3D8R elements. There are 5 elements in the thickness direction. In order to obtain trade-off between computational cost and accuracy, one-eighth of central hole and notched specimens were employed, while one-quarter of Nakajima specimen was adopted. For the in-plane shear specimens, one-half in the thickness direction was performed. The minimum elements size of the central hole specimen, notch specimen, shear specimen, and Nakajima specimen is 0.2 × 0.2 mm, 0.2 × 0.2 mm, 0.15 × 0.15 mm and 0.9 × 0.9 mm, respectively. The predicted load-stroke curves of the related uniaxial tensile tests were obtained, as shown in Fig. 9. Figure 9(b), (d), (f) and (h) show the evolution of stress triaxiality and Load parameter regarding the critical points shown by red dots in Fig. 9(a), (c), (e) and (g), respectively.

In order to determine the fracture strain, the sharp drop of load in the load-stroke curves can be considered as the initiation of fracture. The fracture strains of each test configuration are listed in Table 2.

By indicating the moment when the simulation elongation was approximately equal to the experimental one, the fracture point is defined in simulation [47]. The stress triaxiality and Lode parameter can be further calculated according to the simulated principal stress values. In addition, the average formulation for stress triaxiality and Lode parameter were selected since the stress state was varying in the tension process [34]. The average parameters are defined as follows:

$$\eta_{ave} = \frac{1}{\varepsilon_f} \int_0^{\varepsilon_f} \eta d\varepsilon \tag{7}$$

$$L_{ave} = \frac{1}{\varepsilon_f} \int_0^{\varepsilon_f} L d\varepsilon \tag{8}$$

Using least square method (LSM), the material parameters of MMC fracture criterion were obtained i.e., $K = 663.2$, $c = 1.257$, $\varphi = 0.03897$, $c_\theta^s = 0.002975$, $c_\theta^{ax} = 0.002857$,

$n = 0.05065$. The prediction of three-dimensioned fracture locus was illustrated in Fig. 10.

Consequently, the extended MMC fracture model in predicting fracture strain at room temperature without considering DRX effect can be obtained:

$$\varepsilon_{hLf} = [\frac{663.2}{1.257 \cos 0.03897}(\frac{1}{\sqrt{L^2+3}} + (\eta - \frac{L}{3\sqrt{L^2+3}}) \sin 0.03897)$$
$$(0.002975 + (2 + \sqrt{3})(0.002857 - 0.002975)(\sqrt{L^2 + 3}$$
$$-\sqrt{3}))]^{-\frac{1}{0.05065}} \tag{9}$$

Z parameter calibration

To calibrate the proposed ductile fracture model at elevated temperature, the fracture strain associated with temperature and strain rate in different DRX conditions must be firstly determined. The load-stroke curves for different hot plastic deformation conditions are shown in Fig. 11. The FE simulations of the tensile process under different hot plastic deformation conditions are carried out. In this study, the fracture strain is defined as the equivalent plastic strain (PEEQ) of the largest deformed element. Then the fracture strain obtained from the simulations are shown in Table 3.

Figure 12 shows the true stress–strain curve of 7075 aluminum alloy specimen compressed at different strain rates and temperatures after considering the effect of friction [48]. Obviously, the flow stress depends on strain rate and temperature. Furthermore, the stress is found to decrease with the rising temperature and decreasing strain rate, since higher temperature and lower strain rate supply more time for energy accumulation and grain boundary sliding which leads to the nucleation and growth of recrystallized grains (RGs) as well as annihilation of dislocations. As for each curve, after the flow stress increases rapidly to its peak, it monotonously decreases and reaches a steady state, which usually indicates the beginning of DRX. It can be summarized that the evolution of flow stress was distinguished by three evident stages. At Stage I, the flow stress shows a sharp increasing trend upwards a critical value which indicates strain hardening predominates [49]. Then at stage II, the flow stress exhibits a tender increase until the peak value is reached, which represents the DRX-induced softening. At

Fig. 8 Meshing for specimens with different stress states at room temperature (**a**) Central hole specimen, (**b**) notched specimen, (**c**) shear specimen and (**d**) Nakajima specimen
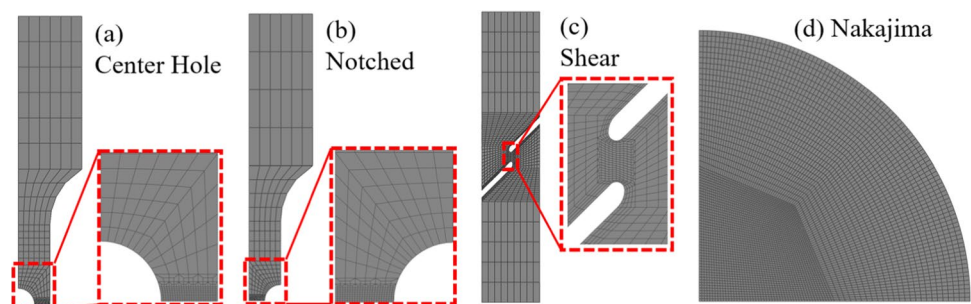
Fig. 9 Evolution of load-stroke and stress states at room temperature (**a**) Load-stroke for central hole specimen, (**b**) stress state of central hole specimen, (**c**) load-stroke of notched specimen, (**d**) stress state of notched specimen, (**e**) load-stroke of sheared specimen, (**f**) stress state of sheared specimen, (**g**) load-stroke of Nakajima specimen and (**h**) stress state of Nakajima specimen (The red dot shows the location of element from which the results in Fig. 9(b), (d), (f) and (h) are obtained)
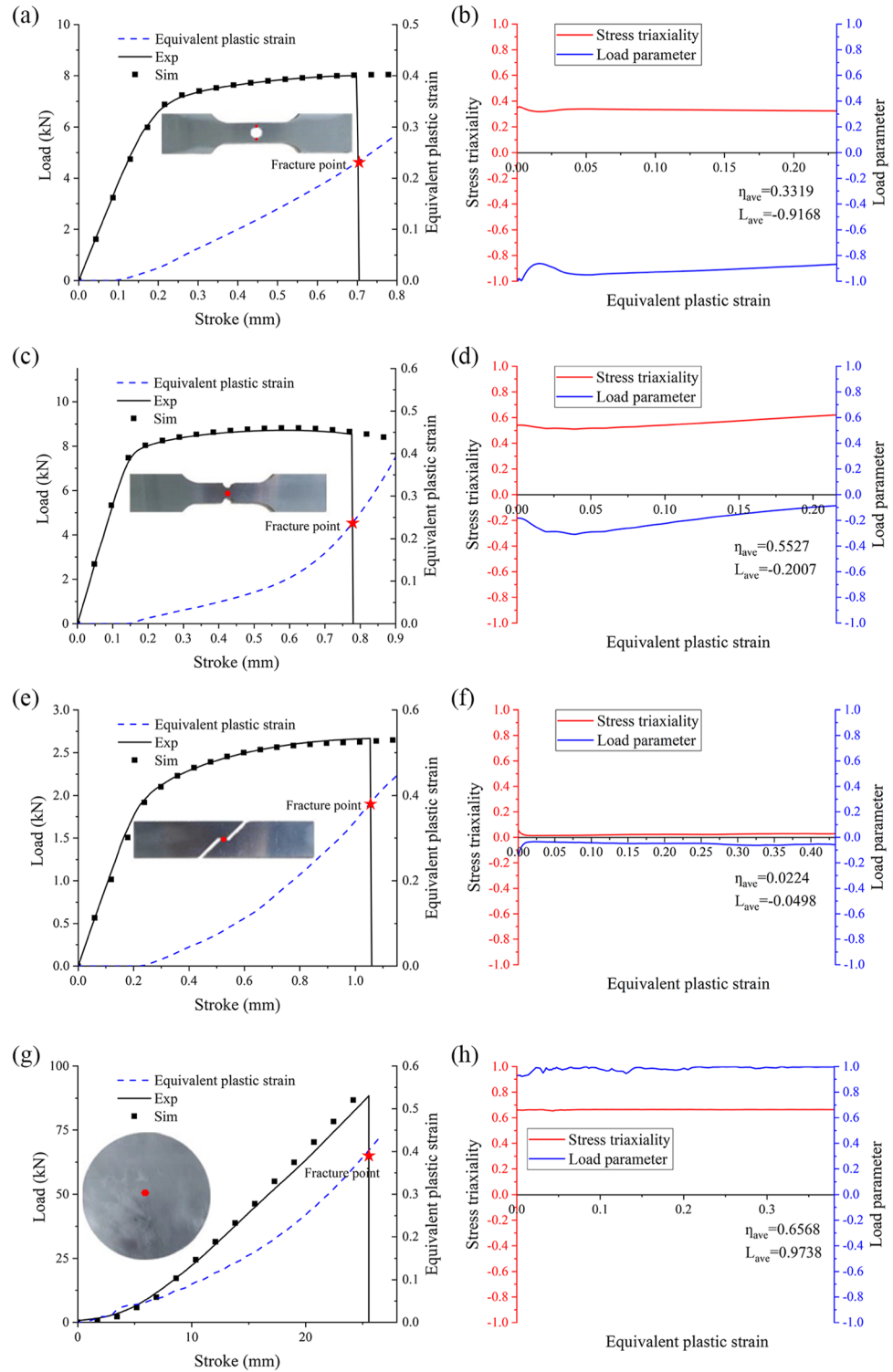
stage III, the flow stress decreases gradually to a stable state with DRX-induced softening. Since at lower strain rates and higher temperatures the higher DRX softening rate decelerates the strain hardening [50], the typical flow stress curves during DRX softening are easier to identify at lower strain rate and higher temperature.

Figure 13 displays the linear relationship between peak stress and strain rate defined in specific forms at different temperatures. The mean slopes of $\ln\left(\sinh\left(\alpha\sigma_p\right)\right)$ vs $1/T$ at peak stress is calculated to obtain the apparent activation energy in hot plastic deformation process, as shown in Fig. 13(d). According to the quantitatively analyzed data, the value of α

Table 2 Stress triaxiality, Lode parameter and fracture strain of 7075 aluminum alloy with various tensile specimens

	Stress triaxiality (η)	Lode parameter (L)	Fracture strain (-)
Central Hole	0.3310	− 0.9122	0.2311
Notched	0.5527	− 0.2007	0.2157
Shear	0.0223	− 0.0498	0.4335
Nakajima	0.6566	0.9738	0.3805

is determined as 0.01005 and the average activation energy for 7075 aluminum alloy is 132.556 kJ/mol. Additionally, partial differentiation of equation will be computed to obtain the apparent activation energy as follows:

$$Q_{drx} = R \left[\frac{\partial \ln \dot{\varepsilon}}{\partial \ln \left(\sin h \left(\alpha \sigma_p \right) \right)} \right]_{T=const} \left[\frac{\partial \ln \left(\sin h \left(\alpha \sigma_p \right) \right)}{\partial (1/T)} \right]_{\dot{\varepsilon}=const} \tag{10}$$

For characterizing DRX initiation, the critical strain and the peak strain are employed as the representative parameters: $\varepsilon_c = 0.03282 Z^{0.02004}$ and $\varepsilon_p = 0.0794 Z^{0.02053}$ (calibration in Appendix A). The microstructure evolution due to DRX in hot plastic deformation process will be evaluated according to the formulation given as follows:

$$X_{drx} = 1 - \exp \left[-0.1906 \left(\frac{\varepsilon - \varepsilon_c}{\varepsilon_p} \right)^{1.6121} \right] \tag{11}$$

To calibrate the material constants k_d, n_d, the deformation parameters related to $X_{drx} = 1$ must be determined, such as the average grain size reaching a constant value and the flow stress coming to a stable state. By substituting the

determined deformation parameters related to $X_{drx} = 1$ into Eq. (11), the mean value of k_d and n_d can be acquired as 0.1906 and 1.6121, respectively. Thus, the volume fraction of DRX computed from the true stress–strain curves during the compressed scenario can be depicted in Fig. 14.

Figure 14 shows the volume fraction of DRX for 7075 aluminum alloy obtained at various temperatures for strain rate of 0.01 s $^{-1}$ and various strain rates for deformation temperature of 723 K. In Fig. 14(a), the strain for the identical volume fraction of DRX increases as the temperature decreases, which indicates as the temperature rises, the recrystallization proceeds continuously [51]. As for a specific temperature in Fig. 14(b), the deformation strain for the same volume fraction of DRX grows with rising strain rate, which indicates that lower strain rate is more favorable for complete DRX. Furthermore, the incomplete DRX tends to occur in hot deformed AA7075 alloy at higher strain rates and lower temperatures because of reduced mobility of grain boundaries.

The relationship between the strain at fracture and Z parameter at various temperatures is shown in Fig. 15. The Z parameter is used to represent the DRX behavior which is related to strain rate and temperature. It is found that the fracture strain has the tendency to decrease approximately monotonically with the rising Z parameter as illustrated in Fig. 15. With the occurrence of DRX during hot tensile tests, refined and equiaxed grains were formed within the fracture region, and the strain at fracture becomes greater than the one at room temperature. From the micro-mechanism view of point, ductile fracture is attributed to the mechanisms of void nucleation, void growth and coalescence. With the increasing DRX volume fraction, the growth of voids is significantly delayed because of the relief of the localized stress concentration induced by the

Fig. 10 Fracture locus of 7075 aluminum alloy predicted by the extended MMC criterion in the space of $\langle \eta, L, \varepsilon_{hLf} \rangle$
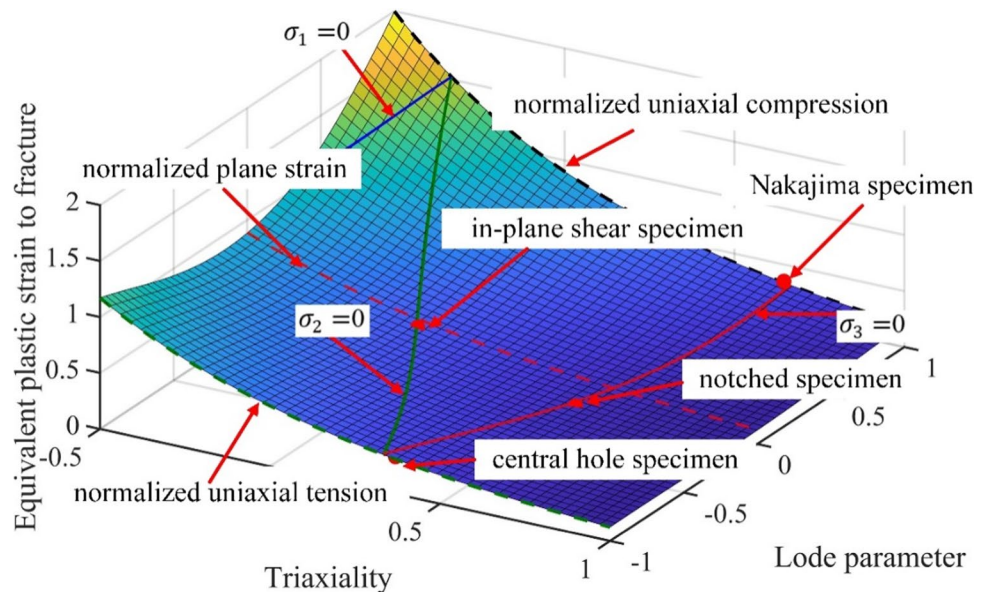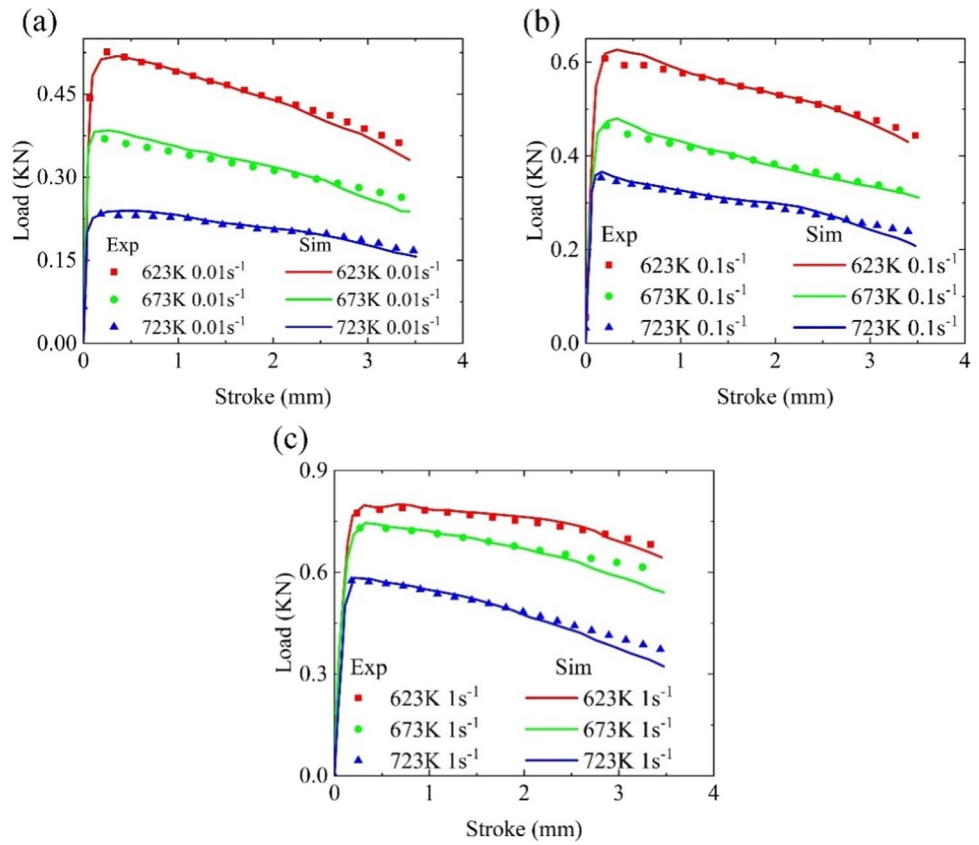
Fig. 11 Comparison of load-stroke between simulation and experiments under different hot plastic deformation conditions

energy-free DRX grains, so the fracture strain increases with rising DRX. Furthermore, in the absence of DRX deformation, the fracture strain is insensitive to the Z parameter and estimates the strain at room temperature. Once DRX occurs, the relationship between the fracture strain and the logarithm of Z can be linearly approximated by Eq. (12):

$$\varepsilon_f = 0.3122[8.8303 - 0.3169 \ln (Z)] \tag{12}$$

Consequently, based on the material parameters calibrated by uniaxial tensile tests at room and elevated temperature summarized in Table 4, the formulation of fracture strain for 7075 aluminum alloy with calibrated material parameters under hot-working conditions is eventually obtained as follows:

Table 3 Fracture strains of 7075 aluminum alloy in varying hot plastic tensile conditions

Temperature (K)	Strain rate $\left(s^{-1}\right)$		
	0.01	0.1	1
623	0.5601	0.3044	0.2972
673	0.7111	0.5065	0.2823
723	0.8821	0.6067	0.3841

$$
\begin{cases}
\varepsilon_{hf} = [\frac{663.2}{1.257\cos 0.03897}(\frac{1}{\sqrt{L^2+3}} + (\eta - \frac{L}{3\sqrt{L^2+3}})\sin 0.03897) \\
\quad (0.002975 + (2+\sqrt{3})(0.002857 - 0.002975)(\sqrt{L^2+3} \\
\quad -\sqrt{3}))]^{-\frac{1}{0.05065}} & \varepsilon < \varepsilon_c \\
\varepsilon_{hf} = [\frac{663.2}{1.257\cos 0.03897}(\frac{1}{\sqrt{L^2+3}} + (\eta - \frac{L}{3\sqrt{L^2+3}})\sin 0.03897) \\
\quad (0.002975 + (2+\sqrt{3})(0.002857 - 0.002975)(\sqrt{L^2+3} \\
\quad -\sqrt{3}))]^{-\frac{1}{0.05065}}\left[(1-X_{drx}) + (8.8303 - 0.3169*\ln(Z))X_{drx}\right] & \varepsilon \ge \varepsilon_c
\end{cases}
\tag{13}
$$

Parameter sensitivity

The proposed MMC criterion at elevated temperature, parameter sensitivity was performed to elaborate the quantitative influence of material parameters on the fracture locus.

Temperature and strain rate

The effect of strain rate on fracture strain is depicted in Fig. 16(a), including the deformations temperature of 673 K and the strain rates of 0.01, 0.1 and 1 s^{-1}. It could be noted in case of the strain rate of 1 s^{-1}, the fracture locus is relatively lower than that of strain rate of 0.01 and 0.1 s^{-1}. This is caused by the fact that the microvoids have sufficient time to nucleate, grow, and coalesce into microcracks at the lower strain rate. Figure 16(b) illustrates the influence of temperature ranging from 627 to 723 K on fracture locus at the strain rate of 0.1 s^{-1}. At high temperature, the

Fig. 12 Schematically shows the flow curves of 7075 aluminum alloy under various temperatures and strain rates

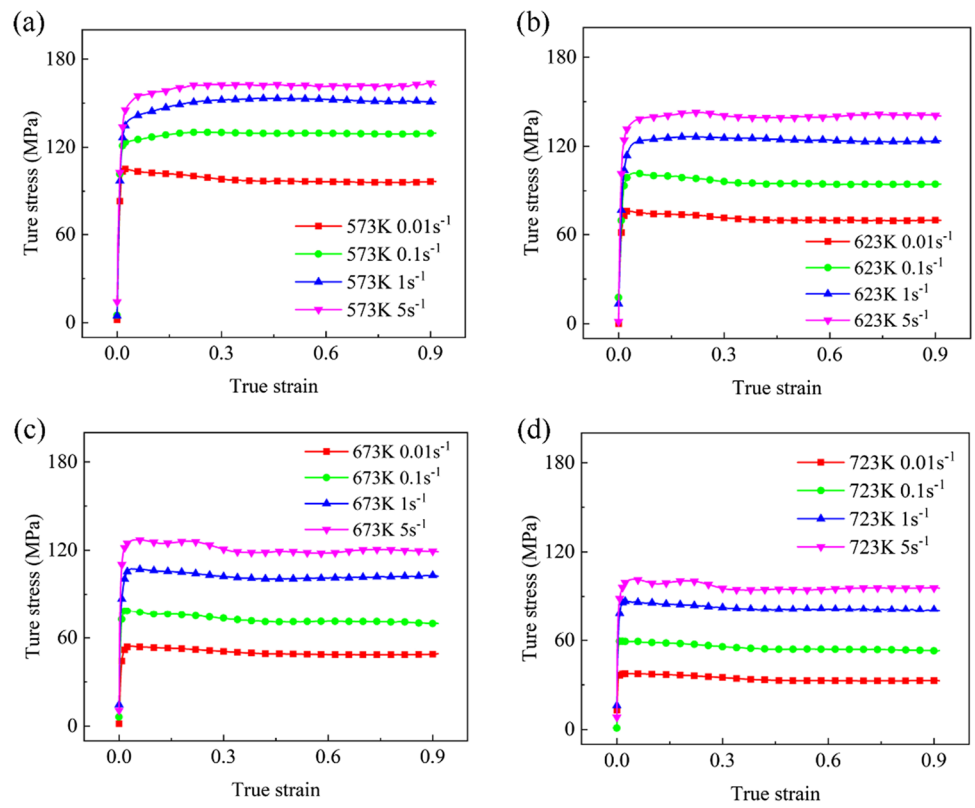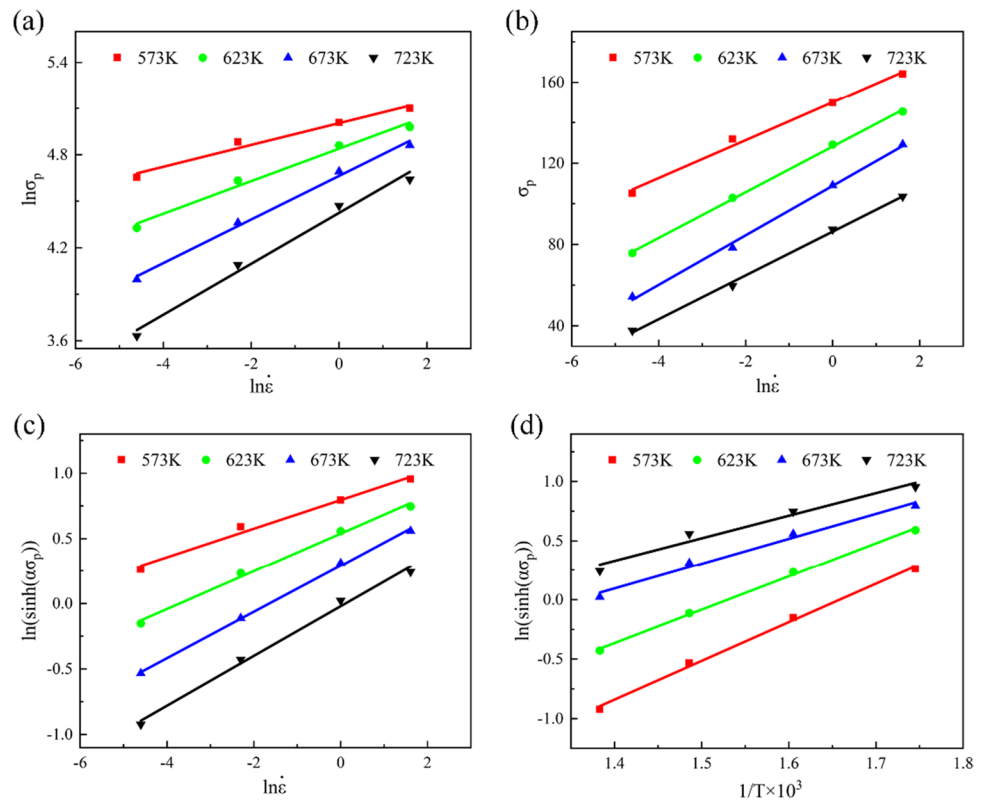**Fig. 13** Determination of constants in Eq. (10) according to the linear relationship of (**a**) $\ln\sigma_p - \ln\dot{\varepsilon}$, (**b**) $\sigma_p - \ln\dot{\varepsilon}$, (**c**)$\ln\left(\sin h\left(\alpha\sigma_p\right)\right) - \ln\dot{\varepsilon}$ and (**d**) $\ln\left(\sin h\left(\alpha\sigma_p\right)\right) - T^{-1}$
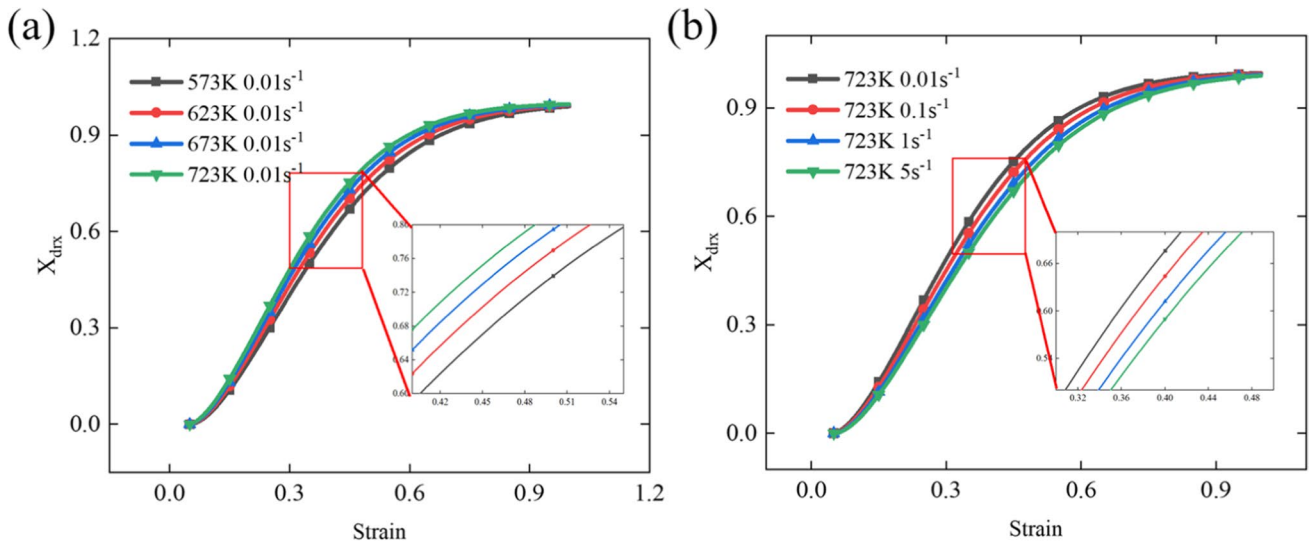
Fig. 14 Volume fraction of DRX for 7075 aluminum alloy obtained from (**a**) Various temperatures at strain rate of 0.01 s $^{-1}$ and under (**b**) various strain rates at temperature of 723 K
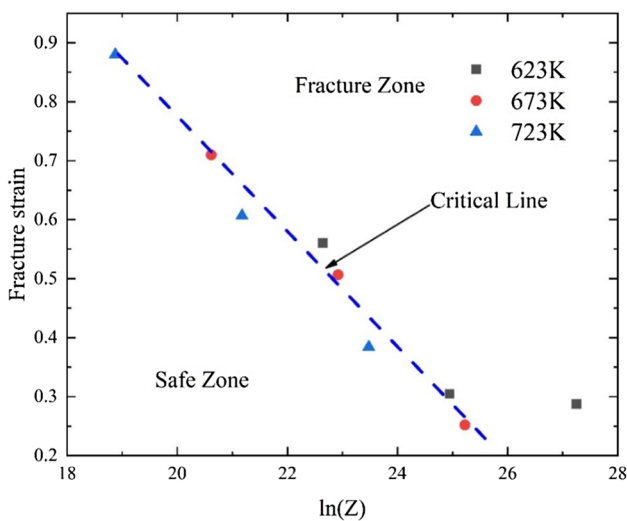
Fig. 15 Linear relationship between the parameter of Z and fracture strain at various temperatures

Table 4 Material parameters of 7075 aluminum alloy

Parameters	Values
K	663.2
c	1.257
φ	0.03897
c_θ^s	0.002975
c_θ^{ax}	0.002857
n	0.05065
A_f	8.8303
B_f	0.3169

thermal motion of atoms in the material intensifies, dislocations are prone to glide and climb, and dynamic recovery (DRV) and DRX are prone to occur, which prolongs the steady-state deformation stage of the material, resulting in higher fracture strain. In the three-dimensional space consisting of stress triaxiality, Lode parameter and fracture strain, the fracture locus at 623 K is lower than the others, and the fracture locus at 723 K is located at the top of these three fracture surfaces.

Stress triaxiality and Lode parameter

After the fracture surfaces are projected onto a two-dimensional plane $L = 0$, the relationship between the ductile fracture strain versus the stress triaxiality is depicted in Fig. 17(a). It denotes the fracture strain decrease with increasing imposed stress triaxiality. Figure 17(b) reflects the projections of fracture surfaces onto the plane $\eta = 0$. Fracture strain decrease initially and then grows with the increase of Lode parameter. Additionally, the minimum value of fracture strain does not occur at $L = 0$, which is consistent with the ductile fracture behavior at room temperature [13].

Model verification

To illustrate the feasibility of the proposed MMC ductile fracture model, FE simulation was employed to predict critical fracture strain. Based on the platform of ABAQUS/Explicit, the numerical implementation of the MMC criterion was conducted using user-defined subroutines. The FE modeling such as element size, boundary conditions and material properties are the same as those depicted in Sect. 4.1.
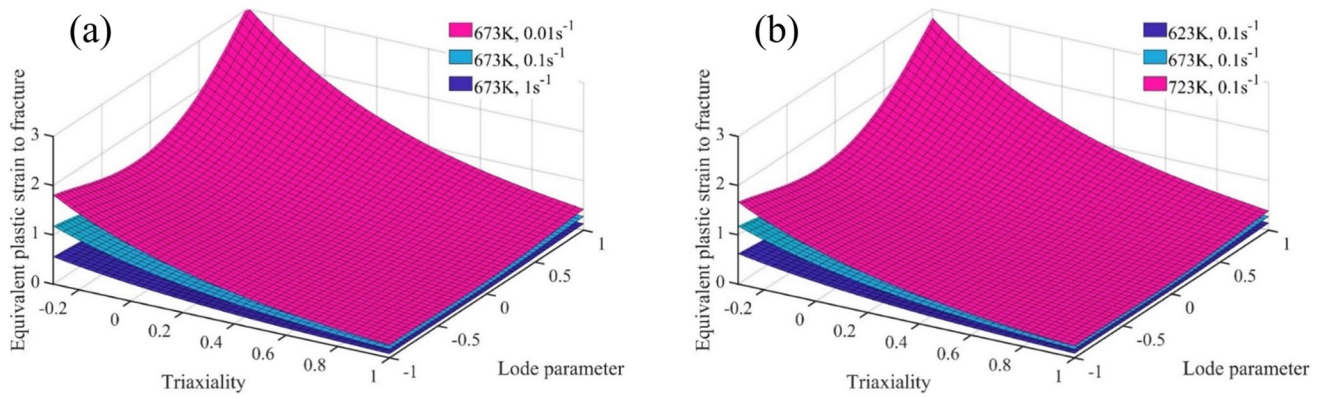
Fig. 16 Fracture locus at various strain rate and temperatures predicted by the extended MMC model (a) Strain rates, (b) temperatures
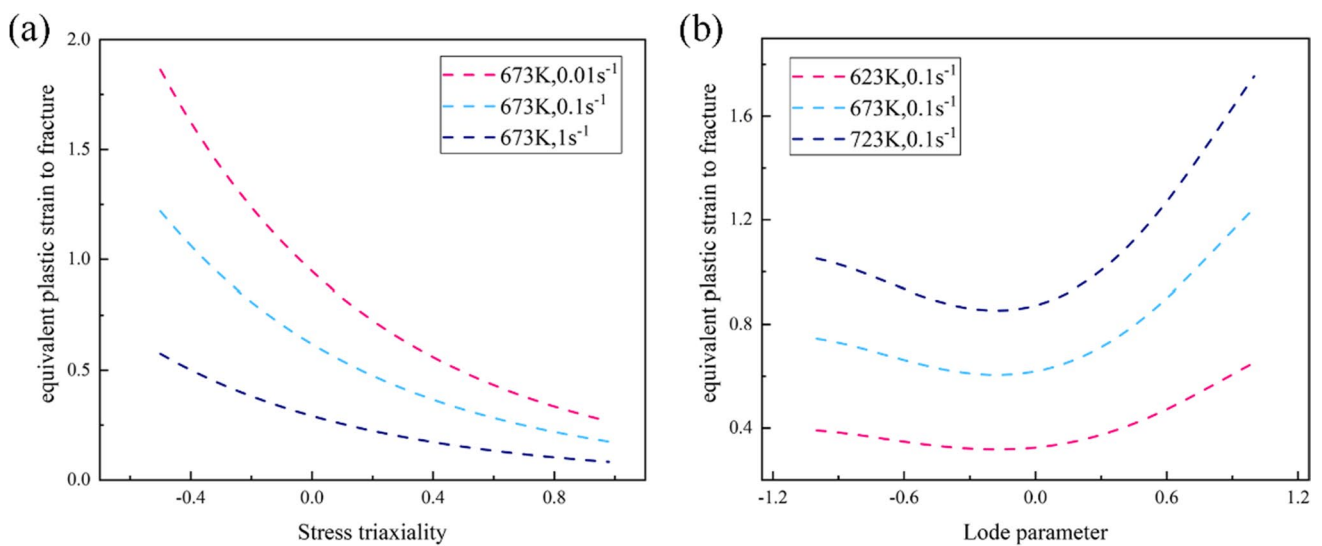

Fig. 17 Influences of stress triaxiality and Lode parameter on fracture strain (a) Strain rates, (b) temperatures

Figure 18 shows the evolutions of state variables at 698 K and 0.05 s^{-1}. Figure 18(a) illustrates the damage distribution of the uniaxial hot tensile specimen in the deformed section. Since the properties of the material are considered to be uniformly distributed during the simulation, and there are no inclusions and voids, the maximum damage takes place at the center of the specimen. As illustrated in Fig. 18(b), the damage factor and fracture strain gradually increase during the tensile process. The damage factor and fracture strain of the central region are higher than the values at the edges, which means that the fracture initiates at the central region. Figure 18(c) depicts the evolution of the stress triaxiality and Lode parameter towards stroke during the hot stretching process. The stress triaxiality and Lode parameter remain stable at the center and gradually increase at the edges, which indicates that the stress state at the center remains constant. Figure 18(d) shows the evolution of Z parameter and DRX. Z parameter remains constant after a sharp increase, which is due to the fact that the Z parameter

is predominately controlled by temperature and strain rate. Since the temperature and strain rate in the deformation region are constant, the Z parameter remains relatively stable.

Application

Set-up of FE simulation

The hot T-shaped forming equipment is composed of a T-shaped die, punch and blank holder, as illustrated in Fig. 19(a). The YZ32-40 hydraulic press with a maximum pressing force of 400 kN (40 tons) was used to supply the forming load. The dimensions of the specimens were depicted in Fig. 19(b). The CAE analysis model of the T-shaped part in hot forming process was developed. In the FE simulation, the tool set was defined as a discrete rigid body, while the blank

Fig. 18 State variables evolution at 698 K-0.05 s^{-1} (**a**) Damage distribution, (**b**) damage factor and fracture strain, (**c**) the stress triaxiality and Lode parameter, (**d**) logarithm of Z parameter and the percentage of DRX
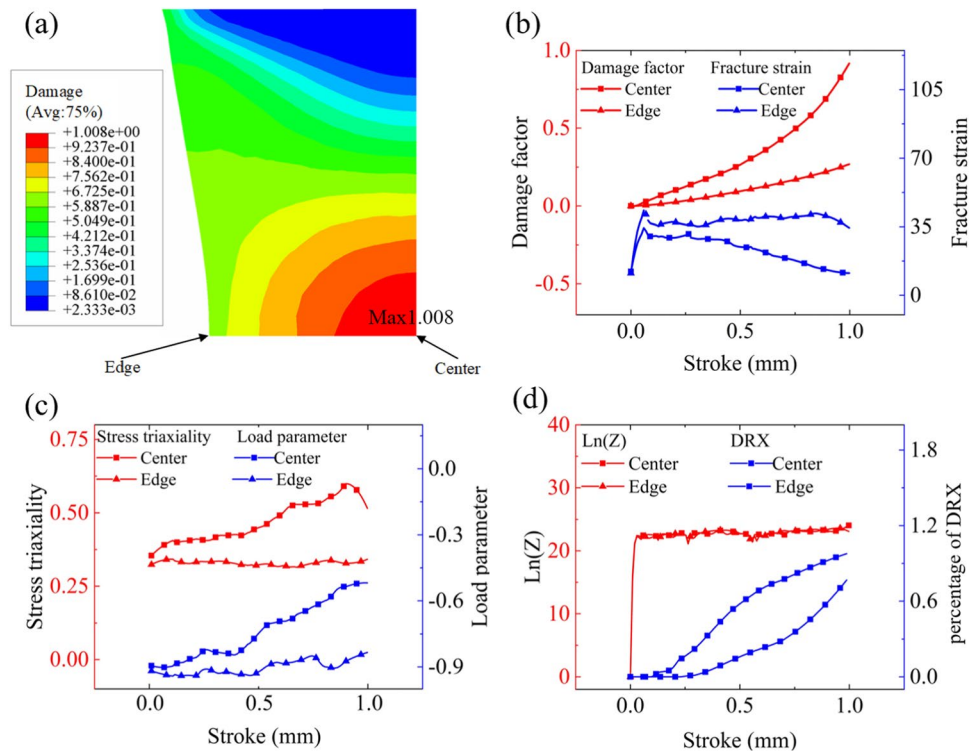
was considered to be a deformable body. To improve computational efficiency, a four-node temperature-coupled shell element called S4RT was used for the die, and the blank was meshed with C3D8RT. The FE model was discretized into 75,213 elements and it is illustrated in Fig. 19(c). The key dimensions of the die cavity are shown in Fig. 19(d).

The physical parameters of 7075 aluminum alloy used in the FE simulations are derived from the previous work of Tang et al. [52]. The coefficient of friction between blank and tools was defined as 0.1. The initial temperature of the blank was set to 673 K, while the tool temperature was 298 K. During the forming process, the punch moved downward with a constant speed of 10 mm/s.

Parameters evolution in the T-shaped forming process

In Fig. 20(a), at the rounded corners, the damage firstly reaches the value of unity, which shows consistency with the experimental results. In order to verify the model more quantitively, the experimental and numerical values of the punch displacement at the onset of fracture are given. It is found that the downward depth of the punch is 9.6 mm in experiments, and the simulated one is 9.4 mm. Considering the acceptable errors in engineering, the accuracy of the simulation results can be verified. In Fig. 20(b), the damage factor gradually increases when the die moves downward. The fracture strain fluctuates during the forming process, showing an overall decreasing trend after reaching the peak value. The magnitude of fracture strain is influenced by several factors such as the stress state

and the degree of DRX. Figure 20(c) shows the stress state of the point with the maximum value of plastic strain. It indicates that the stress triaxiality does not change much during the forming process. In Fig. 20(d), the value of ln(Z) increases sharply at the preliminary stage and then keeps steady, while the percentage of DRX shows a significant increase leading to an increase of fracture strain. Furthermore, when the damage factor is close to the value of unity, the fracture strain decreases significantly, indicating that Lode parameter has a significant influence which has also been validated in the work of Bao [8].

Figure 21 shows the evolution of state variables at the moment of fracture with the temperature of 673 K and the forming speed of 10 mm/s. Figure 21(a) expresses the distribution of damage factors. The damage is mainly distributed at the fillet and side wall of T-shaped parts. Figure 21(b) indicates the distribution of PEEQ. The maximum value of PEEQ is approximately 0.46 at the initiation of fracture. In Fig. 21(c), since the bottom of the T-shaped part finally contacts with the die, its temperature is relatively high. Figure 21(d) illustrates the distribution of volume fraction of DRX. The volume fraction of DRX is mainly distributed in the corner, while the other regions have minor DRX due to small plastic strain.

The influence of process parameters on ductile fracture

Figure 22 illustrates the influence of forming speed on damage evolution of T-shaped parts. The forming temperature is set to 673 K and the friction coefficient is assigned to 0.1. When the

Fig. 19 T-shaped testing
(**a**) Forming equipment, (**b**)
geometric dimensions of the
specimen (mm), (**c**) FE model
of process to form the T-shaped
component, (**d**) key dimensions
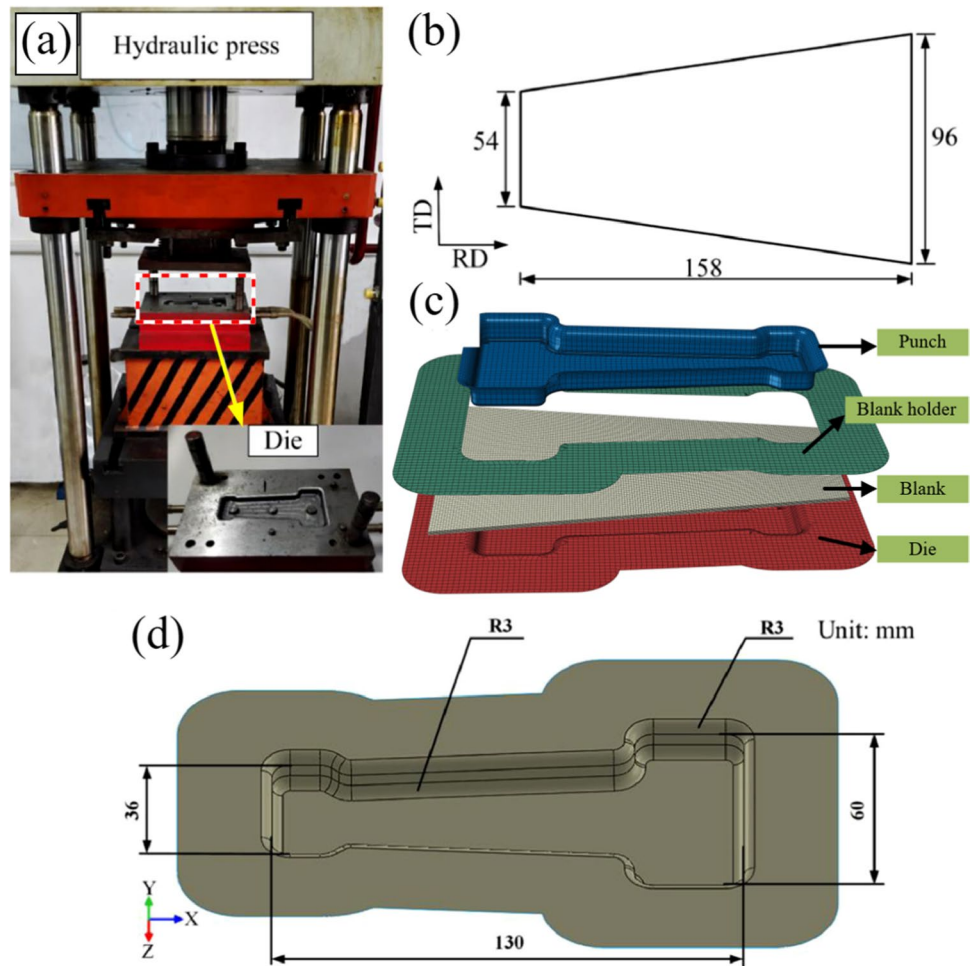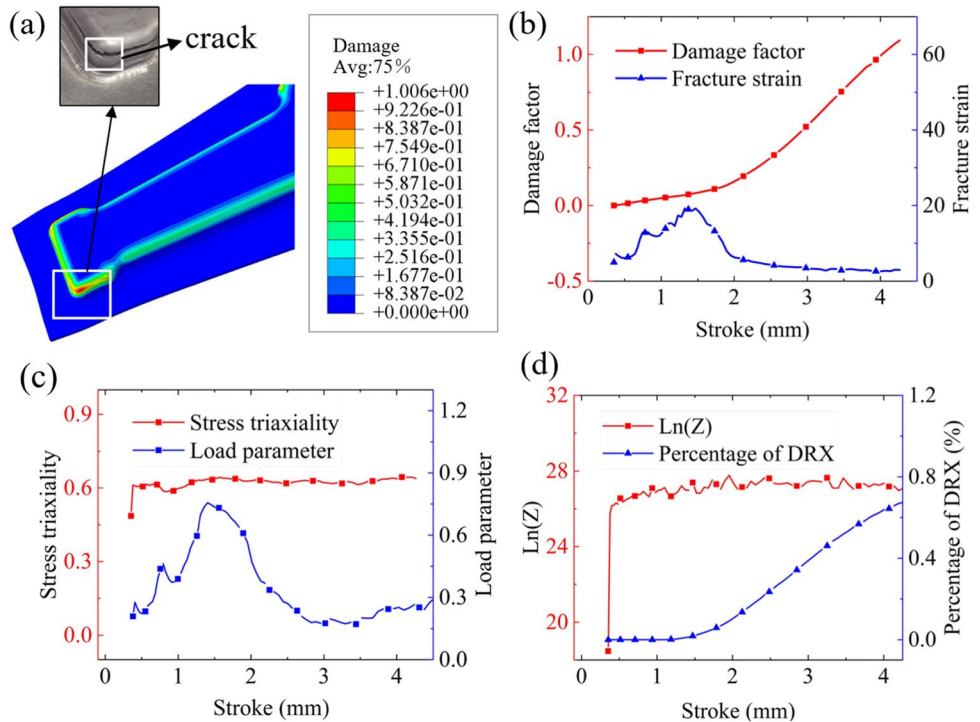of the die cavity

Fig. 20 Parameters evolution in
the T-shaped forming process
(**a**) Damage distribution and
fracture initiation, (**b**) dam-
age factor and fracture strain,
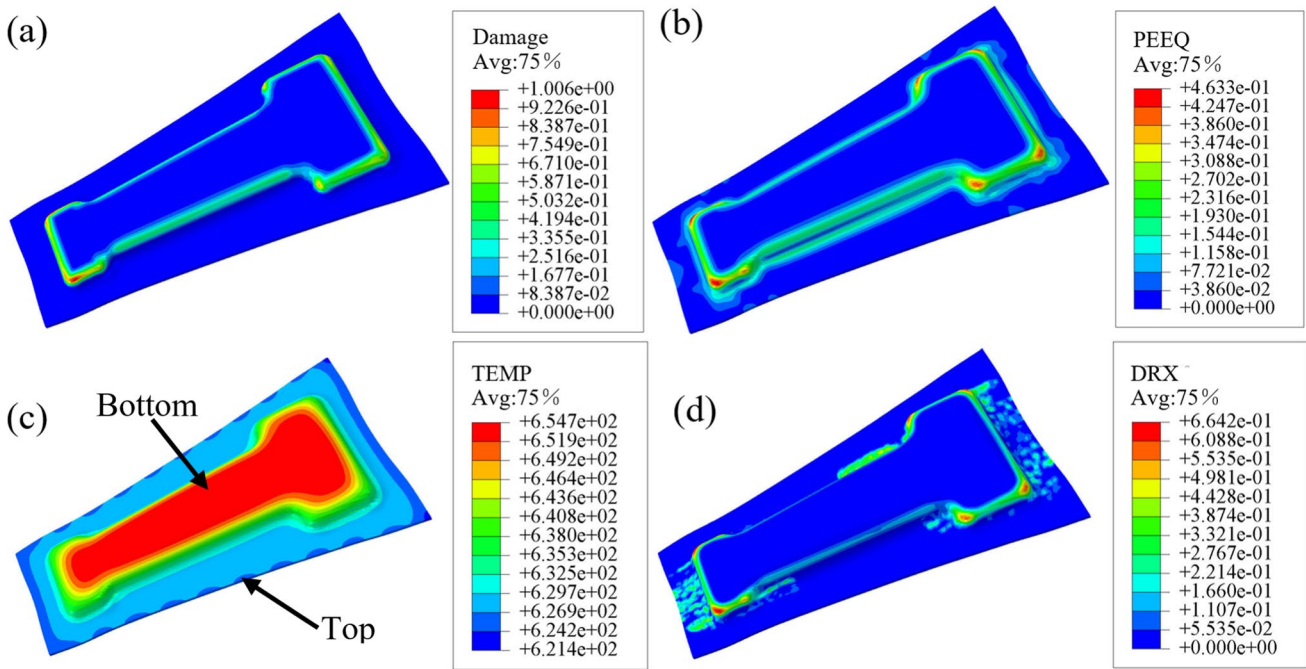(**c**) the stress triaxiality and
Lode parameter, (**d**) ln(Z) and
percentage of DRX

Fig. 21 Evolution of state variables at the moment of fracture for a T-shaped part (**a**) Damage factors, (**b**) PEEQ, (**c**) temperature and (**d**) volume fraction of DRX

forming speed is 4.5, 9, 18, 90 mm/s, the fracture displacement to is 5.49, 4.29, 4.16 and 3.58 mm, respectively. As the forming speed increases, the fracture displacement becomes smaller. Figure 23 displays the distribution of damage during T-shaped forming process at various temperatures. The values of fracture displacements are 4.23, 4.95, 5.49, and 5.82 mm for temperatures 573, 623, 673, and 723 K, respectively. It is attributed to the fact that with increasing testing temperature, softening mechanism such as DRX increases which significantly delays the occurrence of fracture.
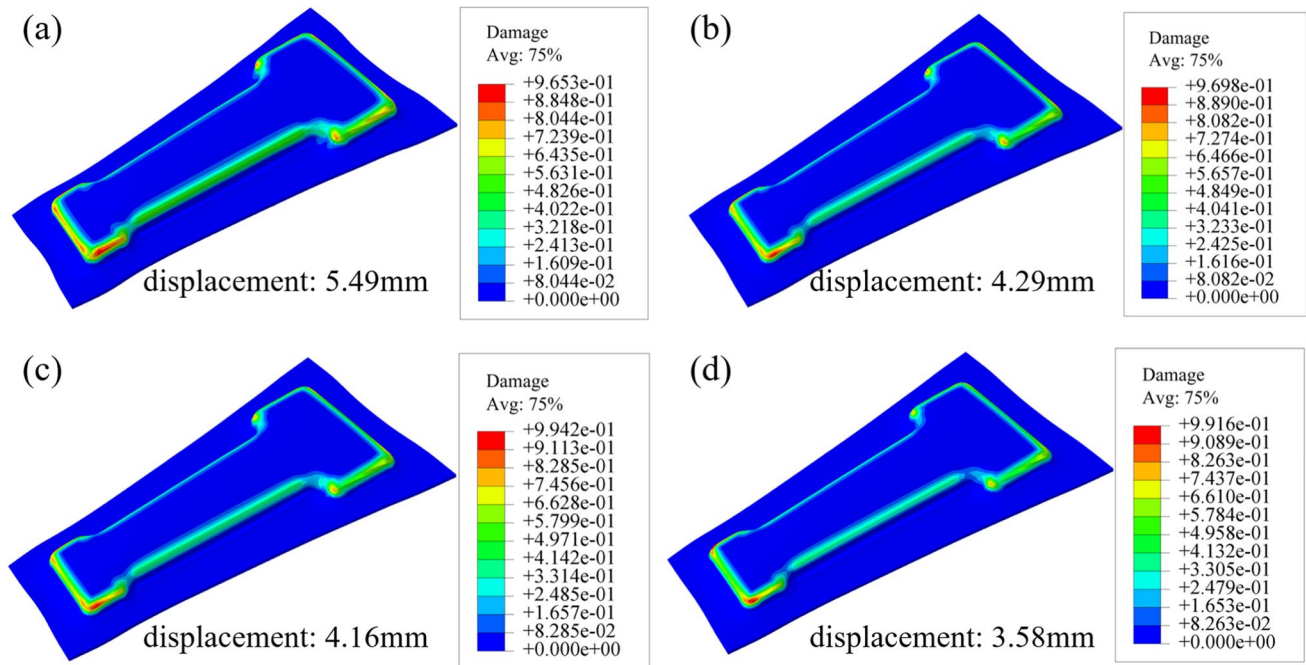
Fig. 22 Damage distribution at the moment of fracture for different stamping speeds (**a**) 4.5 mm/s, (**b**) 9 mm/s, (**c**) 18 mm/s, (**d**) 90 mm/s
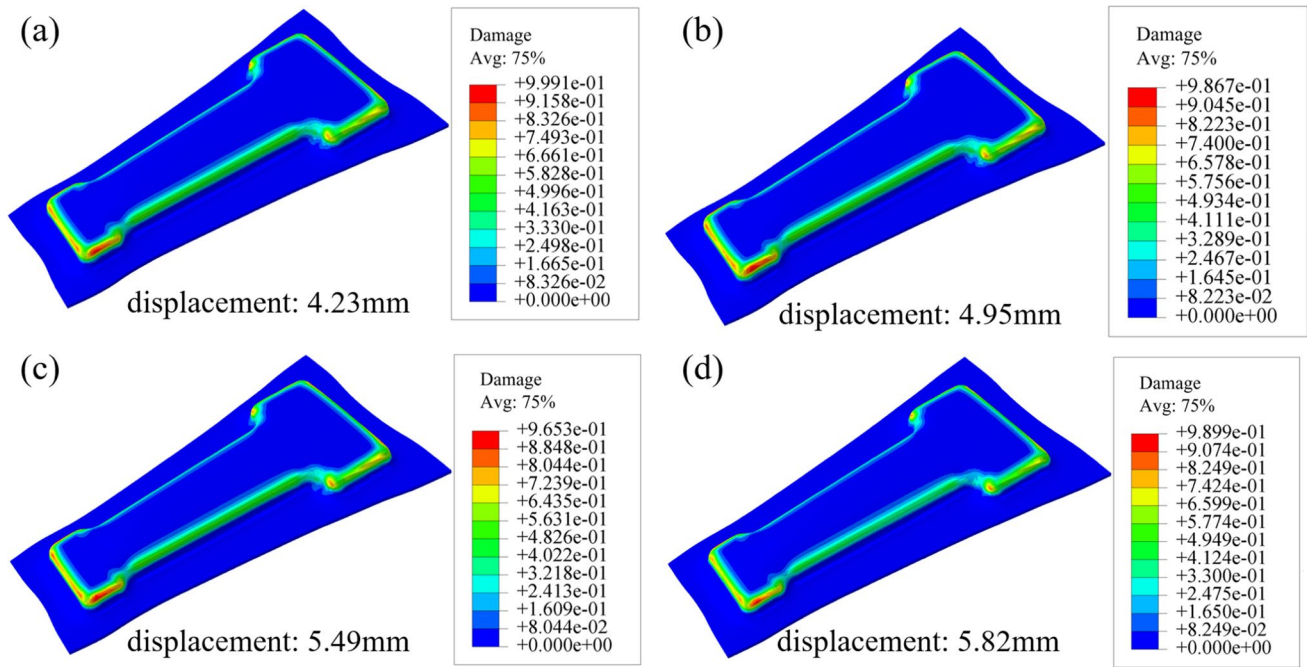
Fig. 23 Damage distribution at the moment of fracture for various temperature (**a**) 573 K, (**b**) 623 K, (**c**) 673 K, (**d**) 723 K

Figure 24 illustrates the evolution of PEEQ under different forming temperatures and forming speeds. Figure 24(a) shows that the fracture strain at 573 K is obviously lower than the that of 623, 673 and 723 K. Figure 24(b) shows that the PEEQ at fracture decreases with the increase of forming speed, indicating that the increasing forming speed makes the premature fracture. In Fig. 25, the damage is affected by forming temperature and speed, and higher speed and lower

temperature make the material more prone to fracture. Figure 26 shows the evolutions of percentage of DRX under different forming temperatures and speeds. The volume fraction of DRX tends to be zero at deformation temperature of 573 and 623 K in Fig. 26(a). With increasing testing temperature, the volume fraction of DRX expresses an obvious increasing trend. In Fig. 26(b), the evolutions of volume fraction of DRX at different forming speeds exhibit similar trend, but a
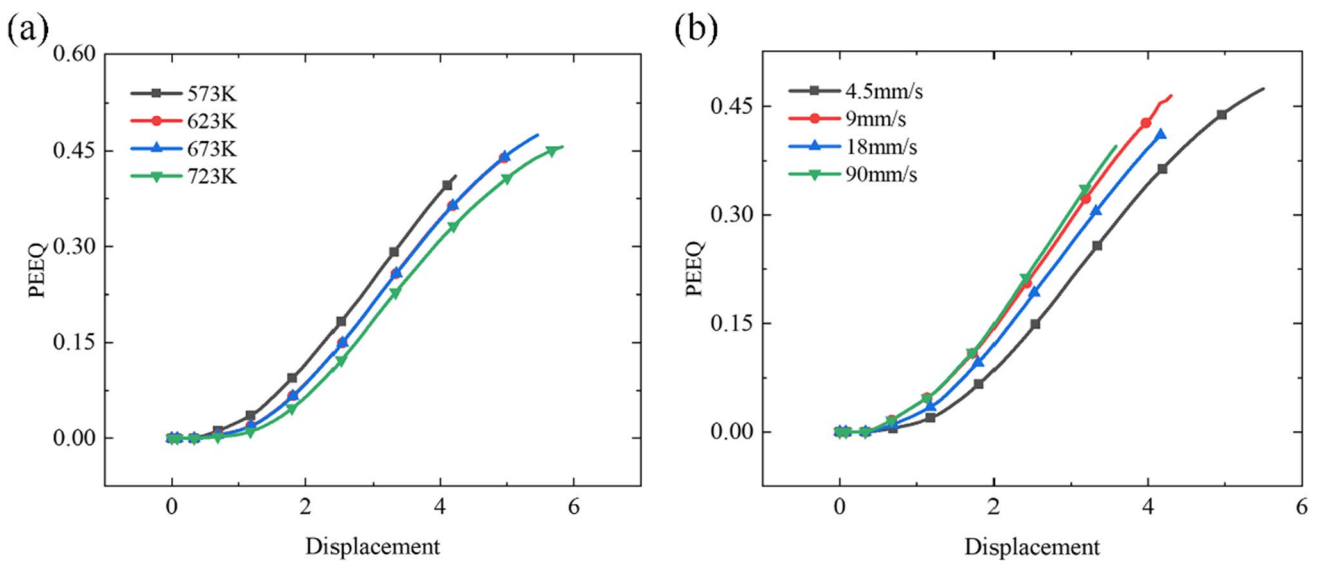

Fig. 24 Evolution of PEEQ under different conditions (**a**) Forming temperatures and (**b**) forming speeds
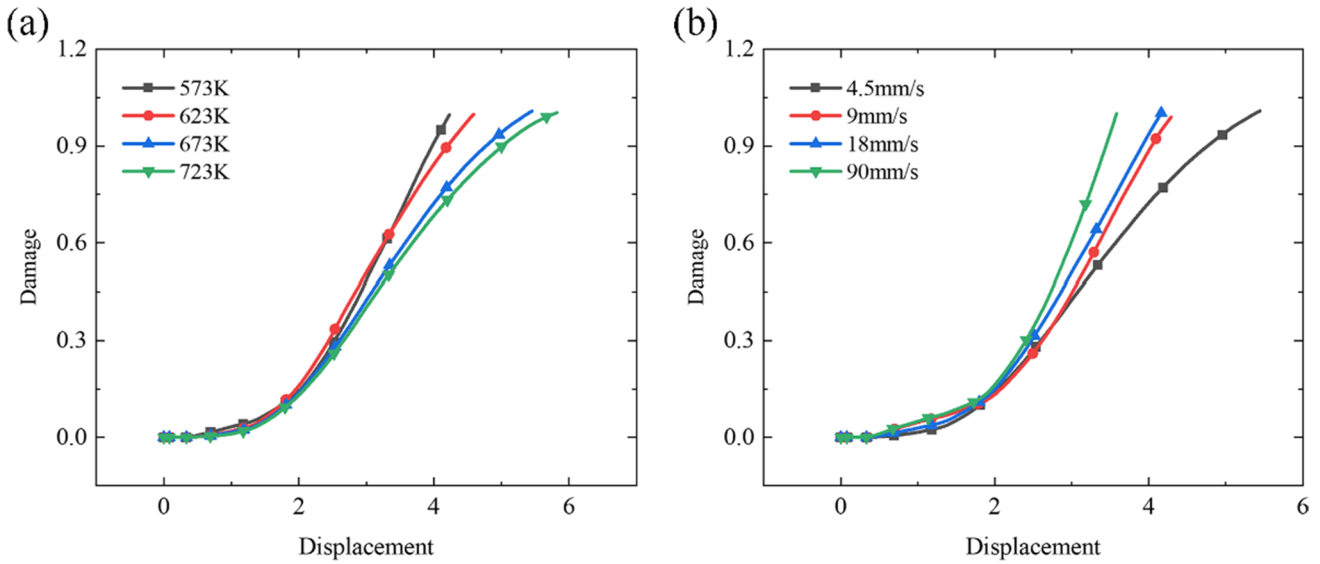
Fig. 25 Evolution of damage under different conditions: (**a**) Forming temperatures and (**b**) forming speeds

higher volume fraction of DRX could be observed at a lower forming speed of 4.5 mm/s due to the sufficient deformation.

Conclusions

In the study, one comprehensive theoretical and experimental investigation on ductile fracture of 7075 aluminum alloy in hot plastic deformation process was provided via proposing an extended MMC model considering the genetic effects of DRX on ductile fracture under various stress states at elevated temperature. The following conclusions can be drawn accordingly.

In order to reveal the effect of stress state on fracture, uniaxial tensile tests with different stress states at room temperature were carried out, and the MMC fracture criterion considering the effect of the stress triaxiality and Lode parameter was established. It was found that the fracture strain decreased with increasing stress triaxiality, and increased initially and then decreased with increasing Lode parameter.

Compression experiments at elevated temperature were conducted to obtain the DRX behavior during plastic deformation process. The volume fraction of DRX gradually grew with increasing strain, and the increase in the DRX with increasing temperature and decreasing strain rate could be witnessed by EBSD characterization. The
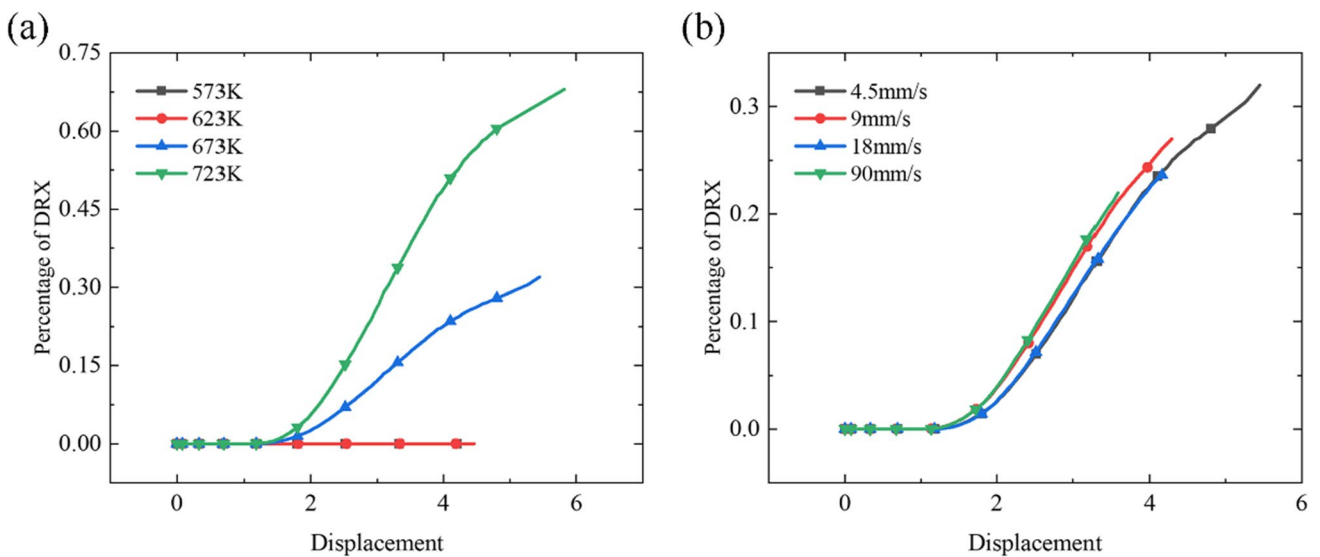

Fig. 26 Evolution of damage under different conditions: (**a**) Forming temperatures and (**b**) for zming speeds
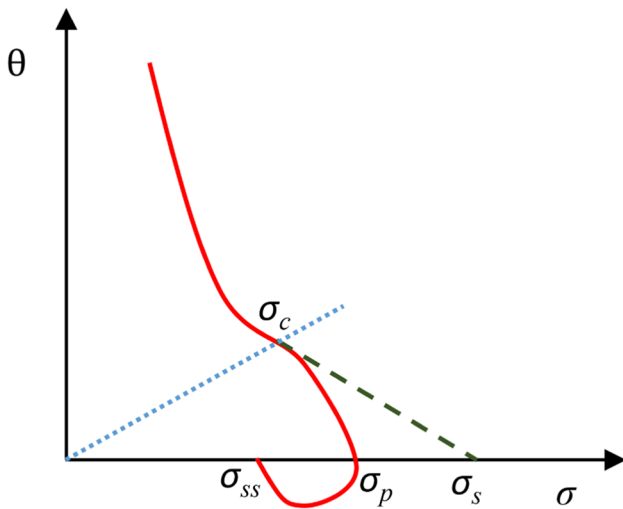
Fig. 27 $\theta - \sigma$ schematic diagram

extended MMC fracture model was established considering the Z parameter and the DRX behavior with various stress states. The fracture strain of AA7075 alloy at varying temperature and stress state was constructed in the coordination of the stress triaxiality and Lode parameter.

The FE simulation of hot tension tests of AA7075 alloy was carried out via the established MMC ductile fracture model, and the parameter evolution was predicted. The volume fraction of DRX increases rapidly with increasing strain, while the volume fraction of DRX at the center was significantly higher

than that at the edges. In the T-shaped parts forming process, the maximum fracture strain can be obtained at a forming speed of 4.5 mm/s and a temperature of 723 K which is caused by the fact that the lower forming speed and higher temperature can significantly increase the softening mechanism such as DRX.

## Appendix A. Z parameter calibration process

In order to determine the characteristic parameters of critical values and peaks applicable to all flow curves studied for 7075 aluminum alloy, a work hardening rate θ ($\theta = \partial\sigma/\partial\varepsilon$) $-\sigma$ curve should be plotted, shown in Fig. 27. The work hardening-stress curves at different temperatures and strain rate are shown in Fig. 28. Using the method proposed in the literature, σ_c is determined as the second derivative of θ relative to σ, that is, the stress value when $\partial^2\theta/\partial\sigma^2$ is 0. The peak stress σ_p is defined as the point at $\theta = 0$. Then, according to the stress–strain curve, the corresponding turning strain ε_c and peak strain σ_p are obtained.

The dynamic recovery softening coefficient Ω is solved by the equation for the work hardening-dynamic recovery stage before the transition strain:

$$\sigma_{WH} = \left[\sigma_s^2 + \left(\sigma_0^2 - \sigma_s^2\right)e^{-\Omega\varepsilon}\right]^{0.5}, \varepsilon < \varepsilon_c \tag{A.1}$$

Starting from Eq. (A.1), the $\ln\Omega - \ln Z$ relationship diagram is drawn as shown in Fig. 29, and the data in Fig. 29 is fitted, then the mathematical model of Ω can be determined as:

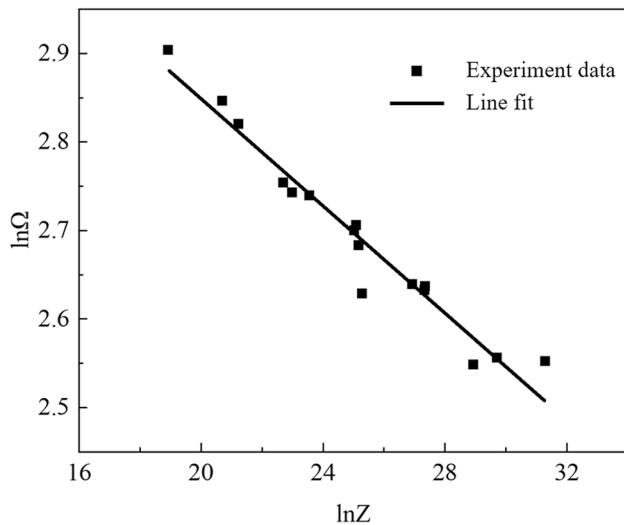**Fig. 28** Work hardening curves of 7075 under different conditions
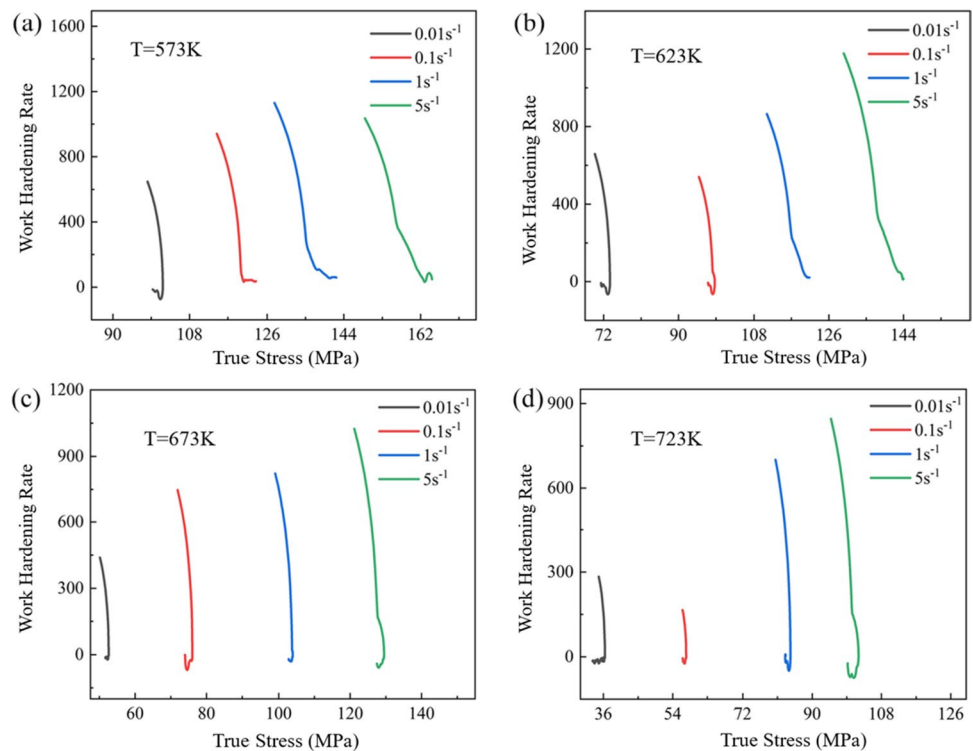
Fig. 29 $\ln\Omega - \ln Z$ schematic diagram

$$\Omega = 14.4846Z^{-0.02851} \tag{A.2}$$

The dynamic recrystallization percentage X_{drx} is usually expressed as:

$$X_{drx} = 1 - exp\left[k_d\left(\frac{\varepsilon - \varepsilon_c}{\varepsilon_p}\right)^{n_d}\right] \tag{A.3}$$

where X_{drx} is the recrystallization volume fraction, k_d and n_d are constants, ε_c is the critical strain, and ε_p is the peak strain. By fitting the experimentally obtained $ln\left(-ln\left(1 - X_{drx}\right)\right)$ and $ln(\varepsilon - \varepsilon_c/\varepsilon_p)$, the values of k_d and n_d can be determined: k_d=−0.1906, n_d=1.6121.

Declarations

Conflicts of interest The authors declare no conflict of interest.

References

1. Cao TS, Gachet JM, Montmitonnet P et al (2014) A Lode-dependent enhanced Lemaitre model for ductile fracture prediction at low stress triaxiality. Eng Fract Mech 124–125:80–96. https://doi.org/10.1016/j.engfracmech.2014.03.021
2. Bonora N, Testa G, Ruggiero A et al (2020) Continuum damage mechanics modelling incorporating stress triaxiality effect on ductile damage initiation. Fatigue Eng Mater Struct 43:13220. https://doi.org/10.1111/ffe.13220
3. Mohr D, Marcadet SJ (2015) Micromechanically-motivated phenomenological Hosford-Coulomb model for predicting ductile fracture initiation at low stress triaxialities. Int J Solids Struct 67–68:40–55. https://doi.org/10.1016/j.ijsolstr.2015.02.024
4. Ma H, Xu W, Jin BC et al (2015) Damage evaluation in tube spinnability test with ductile fracture criteria. Int J Mech Sci 100:99–111. https://doi.org/10.1016/j.ijmecsci.2015.06.005
5. Cockcroft MG, Latham DJ (1968) Ductility and the workability of metals. J of Metals 96:2444
6. Rice JR, Tracey DM (1969) On the ductile enlargement of voids in triaxial stress fields. J Mech Phys Solids 17:201–217. https://doi.org/10.1016/0022-5096(69)90033-7
7. Xue L (2007) Damage accumulation and fracture initiation in uncracked ductile solids subject to triaxial loading. Int J Solids Struct 44:5163–5181. https://doi.org/10.1016/j.ijsolstr.2006.12.026
8. Bai Y, Wierzbicki T (2008) A new model of metal plasticity and fracture with pressure and Lode dependence. Int J Plast 24:1071–1096. https://doi.org/10.1016/j.ijplas.2007.09.004
9. Lou Y, Huh H (2013) Extension of a shear-controlled ductile fracture model considering the stress triaxiality and the Lode parameter. Int J Solids Struct 50:447–455. https://doi.org/10.1016/j.ijsolstr.2012.10.007
10. Lou Y, Huh H, Lim S et al (2012) New ductile fracture criterion for prediction of fracture forming limit diagrams of sheet metals. Int J Solids Struct 49:3605–3615. https://doi.org/10.1016/j.ijsolstr.2012.02.016
11. Lou Y, Yoon JW, Huh H (2014) Modeling of shear ductile fracture considering a changeable cut-off value for stress triaxiality. Int J Plasticity 54:56–80. https://doi.org/10.1016/j.ijplas.2013.08.006
12. Lou Y, Chen L, Clausmeyer T et al (2017) Modeling of ductile fracture from shear to balanced biaxial tension for sheet metals. Int J Solids Struct 112:169–184. https://doi.org/10.1016/j.ijsolstr.2016.11.034
13. Bai Y, Wierzbicki T (2010) Application of extended Mohr-Coulomb criterion to ductile fracture. Int J Fract 161:1–20. https://doi.org/10.1007/s10704-009-9422-8
14. Jia Y, Bai Y (2016) Ductile fracture prediction for metal sheets using all-strain-based anisotropic eMMC model. Int J Mech Sci 115–116:516–531. https://doi.org/10.1016/j.ijmecsci.2016.07.022
15. Jia Y, Bai Y (2016) Experimental study on the mechanical properties of AZ31B-H24 magnesium alloy sheets under various loading conditions. Int J Fract 197:25–48. https://doi.org/10.1007/s10704-015-0057-7
16. Qian L, Fang G, Zeng P (2017) Modeling of the ductile fracture during the sheet forming of aluminum alloy considering nonassociated constitutive characteristic. Int J Mech Sci 126:55–66. https://doi.org/10.1016/j.ijmecsci.2017.03.013
17. Tang B, Wang Q, Guo N et al (2020) Modeling anisotropic ductile fracture behavior of Ti-6Al-4V titanium alloy for sheet forming applications at room temperature. Int J Solids Struct 207:178–195. https://doi.org/10.1016/j.ijsolstr.2020.10.011
18. Qian L, Paredes M, Wierzbicki T et al (2016) Experimental and numerical study on shear-punch test of 6060 T6 extruded aluminum profile. Int J Mech Sci 118:205–218. https://doi.org/10.1016/j.ijmecsci.2016.09.008
19. Cai W, Jiang J, Li G et al (2021) Fracture behavior of high-strength bolted steel connections at elevated temperatures. Eng Struct 245:112817. https://doi.org/10.1016/j.engstruct.2021.112817
20. Cai W, Jiang J, Li G (2021) Analysis and simulation on fracture of structural steel at elevated temperatures based on extended finite element method. Fire Saf J 120:103022. https://doi.org/10.1016/j.firesaf.2020.103022
21. Cai W, Jiang J, Wang Y et al (2020) Fracture behavior of high-strength steels at elevated temperatures. J Constr Steel Res 175:106385. https://doi.org/10.1016/j.jcsr.2020.106385
22. Kacem A, Laurent H, Thuillier S (2022) Experimental and numerical investigation of ductile fracture for AA6061-T6 sheets at room and elevated temperatures. Int J Mech Sci 222:107201. https://doi.org/10.1016/j.ijmecsci.2022.107201

23. Tian X, Guo J (2022) Dynamic mechanical properties and modification of fracture criteria of 6061–T651 aluminum alloy. Eng Fract Mech 262:108273. https://doi.org/10.1016/J.ENGFRACMECH.2022.108273

24. Jia W, Ma L, Jiao M et al (2020) Fracture criterion for predicting edge-cracking in Hot rolling of twin-roll casted AZ31 Mg alloy. J Mater Res Technol 9:4773–4787. https://doi.org/10.1016/j.jmrt.2020.02.103

25. Ning F, Zhou X, Le Q et al (2020) Fracture and deformation characteristics of AZ31 magnesium alloy plate during tension rolling. Mater Today Commun 24:101129. https://doi.org/10.1016/j.mtcomm.2020.101129

26. Zhang X, Zeng W, Shu Y et al (2009) Fracture criterion for predicting surface cracking of Ti40 alloy in hot forming processes. T Nonferr Metal Soc 19:5. https://doi.org/10.1016/S1003-6326(08)60263-0

27. Hashemi SJ, Naeini HM, Liaghat GH et al (2015) Prediction of bulge height in warm hydroforming of aluminum tubes using ductile fracture criteria. Arch Civ Mech Eng 15:19–29. https://doi.org/10.1016/j.acme.2014.08.003

28. Kim WJ, Kim WY, Kim HK (2010) Hot-air forming of Al-Mg-Cr alloy and prediction of failure based on Zener-Holloman parameter. Met Mater Int 16:895–903. https://doi.org/10.1007/s12540-010-1207-0

29. Shang X, Cui Z, Fu MW (2018) A ductile fracture model considering stress state and Zener-Hollomon parameter for hot deformation of metallic materials. Int J Mech Sci 144:800–812. https://doi.org/10.1016/j.ijmecsci.2018.06.030

30. Dehghan-Manshadi A, Barnett MR, Hodgson PD (2008) Hot deformation and recrystallization of austenitic stainless steel: Part I. Dynamic Recrystallization Metall Mater Trans 39:1359–1370. https://doi.org/10.1007/s11661-008-9512-7

31. Zhang J, Li Z, Wen K et al (2019) Simulation of dynamic recrystallization for an Al-Zn-Mg-Cu alloy using cellular automaton. Prog Nat Sci: Mater Int 29:477–484. https://doi.org/10.1016/j.pnsc.2019.04.002

32. Wang S, Luo J, Hou L et al (2016) Physically based constitutive analysis and microstructural evolution of AA7050 aluminum alloy during hot compression. Mater Des 107:277–289. https://doi.org/10.1016/j.matdes.2016.06.023

33. Xiao X, Mu Z, Pan H et al (2018) Effect of the Lode parameter in predicting shear cracking of 2024–T351 aluminum alloy Taylor rods. Int J Impact Eng 120:185–201. https://doi.org/10.1016/j.ijimpeng.2018.06.008

34. Xiao X, Wang Y, Vershinin VV et al (2019) Effect of Lode angle in predicting the ballistic resistance of Weldox 700 E steel plates struck by blunt projectiles. Int J Impact Eng 128:46–71. https://doi.org/10.1016/j.ijimpeng.2019.02.004

35. Wang X, Zhang Y, Ma X (2020) High temperature deformation and dynamic recrystallization behavior of AlCrCuFeNi high entropy alloy. Mater Res Express 778:139077. https://doi.org/10.1016/j.msea.2020.139077

36. Liu J, Wang X, Liu J et al (2019) Hot deformation and dynamic recrystallization behavior of Cu-3Ti-3Ni-0.5Si alloy. J Alloys Compd 782:224–234. https://doi.org/10.1016/j.jallcom.2018.12.212

37. Ban Y, Zhang Y, Tian B et al (2020) EBSD analysis of hot deformation behavior of Cu-Ni-Co-Si-Cr alloy. Mater Charact 169:110656. https://doi.org/10.1016/j.matchar.2020.110656

38. Wu S, Liu Z, Huang X et al (2021) Process parameter optimization and EBSD analysis of Ni60A-25% WC laser cladding. Int J Refract Hard Met 101:105675. https://doi.org/10.1016/j.ijrmhm.2021.105675

39. Dalai B, Moretti MA, Kerstrm P et al (2021) Mechanical behavior and microstructure evolution during deformation of AA7075-T651. Mater Sci Eng A 822:141615

40. Johnson GR, WH C (1983) A constitutive model and data for materials subjected to large strains, high strain rates, and high temperatures. Eng Fract Mech 541–547.

41. Hu M, Sun Y, He J et al (2022) Hot deformation behaviour and microstructure evolution of Al-3%Mg2Si alloy. Mater Charact 183:111623. https://doi.org/10.1016/j.matchar.2021.111623

42. Huang W, Chen J, Zhang R et al (2022) Effect of deformation modes on continuous dynamic recrystallization of extruded AZ31 Mg alloy. J Alloys Compd 897:163086. https://doi.org/10.1016/j.jallcom.2021.163086

43. Lin X, Huang H, Yuan X et al (2022) Study on high-temperature deformation mechanical behavior and dynamic recrystallization kinetics model of Ti-47.5Al-2.5V-1.0Cr-0.2Zr alloy. J Alloys Compd 891:162105. https://doi.org/10.1016/j.jallcom.2021.162105

44. Fan H, Jiang H, Dong J et al (2019) An optimization method of upsetting process for homogenized, nickel-based superalloy Udimet 720Li ingot considering both cracking and recrystallization. J Mater Process Technol 269:52–64. https://doi.org/10.1016/j.jmatprotec.2019.01.013

45. Mofarrehi M, Javidani M, Chen XG (2022) Effect of Mn content on the hot deformation behavior and microstructure evolution of Al–Mg–Mn 5xxx alloys. Mater Res Express 845:143217. https://doi.org/10.1016/j.msea.2022.143217

46. Lou Y, Huh H (2013) Prediction of ductile fracture for advanced high strength steel with a new criterion: experiments and simulation. J Mater Process Technol 213:1284–1302. https://doi.org/10.1016/j.jmatprotec.2013.03.001

47. Kacem A, Laurent H, Thuillier S (2021) Influence of experimental boundary conditions on the calibration of a ductile fracture criterion. Eng Fract Mech 248:107686. https://doi.org/10.1016/j.engfracmech.2021.107686

48 Ebrahimi R, Najafizadeh A (2004) A new method for evaluation of friction in bulk metal forming. J Mater Process Technol 152:136–143. https://doi.org/10.1016/j.jmatprotec.2004.03.029

49. Wan P, Kang T, Li F et al (2021) Dynamic recrystallization behavior and microstructure evolution of low-density high-strength Fe–Mn–Al–C steel. J Mater Res Technol 15:1059–1068. https://doi.org/10.1016/j.jmrt.2021.08.079

50. Xu Y, Chen C, Zhang X et al (2018) Dynamic recrystallization kinetics and microstructure evolution of an AZ91D magnesium alloy during hot compression. Mater Charact 145:39–52. https://doi.org/10.1016/j.matchar.2018.08.028

51. Quan G, Mao Y, Li G et al (2012) A characterization for the dynamic recrystallization kinetics of as-extruded 7075 aluminum alloy based on true stress–strain curves. Comput Mater Sci 55:65–72. https://doi.org/10.1016/j.commatsci.2011.11.031

52. Tang B, Li H, Guo N et al (2021) Revealing ductile/quasi-cleavage fracture and DRX-affected grain size evolution of AA7075 alloy during hot stamping process. Int J Mech Sci 212:106243. https://doi.org/10.1016/j.ijmecsci.2021.106843